A 3D-shell model of left atrial electromechanics

Oscar Ruz, Carlos Brito-Pacheco, Marina Vidrascu, Dominique Chapelle, Miguel Angel Fernández

A 3D-Shell Model of Left Atrial Electromechanics

Oscar Ruz[1,2], Carlos Brito-Pacheco[2], Marina Vidrascu[2], Dominique Chapelle[3], Miguel A. Fernández[2*]

[1]Universidad de Santiago de Chile, Santiago, Chile.
[2]Sorbonne Université, CNRS, LJLL, Inria, Paris, France.
[3]Inria & CMAP, CNRS, Ecole Polytechnique, Institut Polytechnique de Paris, Palaiseau, France.

*Corresponding author(s). E-mail(s): miguel.fernandez@inria.fr;
Contributing authors: oscar.ruz@usach.cl; carlos.brito-pacheco@inria.fr;
marina.vidrascu@inria.fr; dominique.chapelle@inria.fr;

Abstract

The thin-walled nature of the atrial myocardium can lead to artificial stiffening when full 3D electromechanical models are discretized using standard finite elements. In this work, we propose an electromechanical model of the left atrium based on a 3D-shell formulation that overcomes these limitations. The model incorporates both passive and active components of atrial tissue mechanics, while atrioventricular interaction is described by the coupling with a 0D electromechanical model of the left ventricle. The proposed approach is assessed under physiological and pathological conditions and systematically compared with the standard full 3D formulation. The results demonstrate the superior robustness and computational efficiency of the proposed 3D-shell electromechanical model.

Keywords: Cardiac mechanics, Left atrium, 3D-shell model, Lumped-parameter model, Finite element method.

1 Introduction

Computational modeling of cardiac electromechanics has become an essential tool in the analysis of heart function. Such simulations provide quantitative insights into internal mechanical variables that cannot be accessed non-invasively and enable in-silico evaluation of therapeutic strategies and device performance (see, e.g., [1–5]).

The underlying mathematical models must capture the detailed multiscale and multiphysics processes that govern cardiac function, such as electrical activation, active and passive tissue mechanics and coupling with blood flow. The atria contribute to ventricular filling in three distinct ways: by acting as a reservoir during ventricular systole, by allowing passive blood flow into the ventricles during early diastole, and by augmenting ventricular filling during late diastole thanks to atrial contraction. Atrial anatomy is highly complex, with markedly heterogeneous wall thickness that can be as low as 0.5 mm (see, e.g., [6, 7]). Anatomically detailed geometric models with spatially varying wall thickness can be obtained from CT imaging data (see, e.g., [6]). In contrast to the ventricles, atrial myocardial fiber architecture is considerably more complex and does not appear to follow a simple pattern. Moreover, the thin-walled nature of the atrial myocardium complicates the acquisition of patient-specific fiber data (see, e.g., [8]). Rule-based methods are a widely used approach for prescribing realistic fiber orientations in computational atrial geometries (see, e.g., [9–16]).

While ventricular electromechanical modeling has been extensively studied over the past two decades (see, e.g., [17–28]), the literature on atrial mechanics remains comparatively scarce. The first mechanical models of the atria treated the myocardial tissue as a purely passive material, neglecting its contractile function (see, e.g., [29–32]). Only recently has atrial contraction begun to receive significant attention (see [8, 33–46]). Several of these studies have demonstrated good agreement with key physiological indicators, such as the characteristic figure-eight shape of the pressure-volume loop. However, the vast majority of these works disregard the numerical challenges associated with the thin-walled nature of the atrial myocardium. Indeed, with the exception of the studies reported in [29, 33], which are based on a Reissner-Mindlin shell formulation, all the aforementioned approaches model atrial tissue using a standard displacement-based 3D formulation, as commonly done for ventricular myocardium.

Standard finite element approximations of displacement-based 3D solid mechanics models are known to suffer from severe robustness issues, namely artificial stiffening, when the thickness is small compared to the other characteristic dimensions. This so-called numerical locking phenomenon often necessitates highly refined meshes, thereby leading to prohibitive high computational costs. A well-established strategy in solid mechanics to circumvent these issues is to adopt reduced-order modeling approaches based on shell theory, combined with appropriate techniques to mitigate numerical locking (see, e.g., [47, 48] and the references therein). In particular, 3D-shell elements with quadratic shape functions through the thickness are particularly appealing, as they allow for an accurate representation of transverse strains, enable the use of general constitutive laws and facilitate coupling with surrounding media (see [48]).

In this paper, we introduce an electromechanical model of the left atrium based on the 3D-shell formulation introduced in [48]. Additionally, a Mixed Interpolation of Tensorial Components (MITC) reinterpolation technique is considered to mitigate potential locking effects, which are common in thin-walled solid mechanics models (see, e.g., [49]). In order to account for atrioventricular interaction, the atrial model is coupled with a reduced 0D model of the left ventricle electromechanics [50]. The capabilities of the proposed approach are investigated through a series of numerical

experiments under physiological and pathological conditions, and comparisons are also made with a standard displacement-based 3D solid model.

A preliminary version of this work was presented in the FIMH conference paper [51]. The present study significantly extends that contribution in several aspects. First, atrial mechanics are coupled with a 0D reduced-order electromechanical model of the left ventricle, resulting in a more physiologically consistent description of the inter-chamber pressure-volume interaction. Second, mitral valve motion is incorporated through viscoelastic Robin-type boundary conditions. Finally, the proposed 3D-shell formulation is systematically assessed through qualitative and quantitative comparisons with standard full 3D finite element formulations. This includes a comprehensive set of physiological biomarkers, such as atrial stroke work, ejection fraction and pressure-volume loops.

2 Materials and Methods

In this section, we provide the detailed formulation of the left atrial electromechanical model. We introduce the geometric setting, kinematic variables, and the Lagrangian framework, followed by the passive and active constitutive laws and the equations governing the contractile dynamics. Finally, the numerical discretization of the resulting coupled nonlinear problem is presented.

2.1 Electromechanical model of the left atrium

We consider a 3D anatomical geometry of the left atrium represented by a domain $\Omega \subset \mathbb{R}^3$ in its reference configuration (see Figure 1). Its boundary $\partial\Omega$ is assumed to be partitioned into four disjoint parts, $\partial\Omega = \Gamma_{\text{vs}} \cup \Gamma_{\text{mv}} \cup \Gamma_{\text{en}} \cup \Gamma_{\text{ep}}$, where Γ_{vs} corresponds to the pulmonary-vein inlets, Γ_{mv} to the mitral-valve annulus interfacing with the left ventricle, and Γ_{en} and Γ_{ep} denote the endocardial and epicardial surfaces, respectively. The exterior unit normal vector to $\partial\Omega$ is denoted by $\boldsymbol{n}$. The mechanical response of the atrial cardiac tissue will be described using a total Lagrangian framework. To this purpose, we let $\boldsymbol{\varphi} : \Omega \times \mathbb{R}^+ \to \mathbb{R}^3$ denote the motion map, assigning at each material point $\boldsymbol{x} \in \Omega$ its position $\boldsymbol{\varphi}(\boldsymbol{x}, t)$ in the current configuration at time $t \geq 0$. The associated displacement field is defined by $\boldsymbol{y}(\boldsymbol{x}, t) \stackrel{\text{def}}{=} \boldsymbol{\varphi}(\boldsymbol{x}, t) - \boldsymbol{x}$. The associated deformation gradient, characterizing the local stretch and rotation of material line elements, is given by $\boldsymbol{F} \stackrel{\text{def}}{=} \boldsymbol{\nabla}\boldsymbol{\varphi}$, while the Jacobian $J \stackrel{\text{def}}{=} \det \boldsymbol{F}$ represents the local volume ratio between the deformed and reference configurations. We shall also make use of the right Cauchy-Green strain tensor given by $\boldsymbol{C} \stackrel{\text{def}}{=} \boldsymbol{F}^\top \boldsymbol{F}$.

To model the constitutive material behavior, we adopt the multiscale electromechanical framework introduced in [23], which couples the passive and active mechanisms of the cardiac tissue, capturing their interaction through the nonlinear Hill–Maxwell extension. This results in the following additive decomposition of the second Piola-Kirchhoff stress tensor $\boldsymbol{\Sigma}$:

$$\boldsymbol{\Sigma} \stackrel{\text{def}}{=} \boldsymbol{\Sigma}_{\text{p}} + \boldsymbol{\Sigma}_{\text{a}} \quad \text{in} \quad \Omega,$$

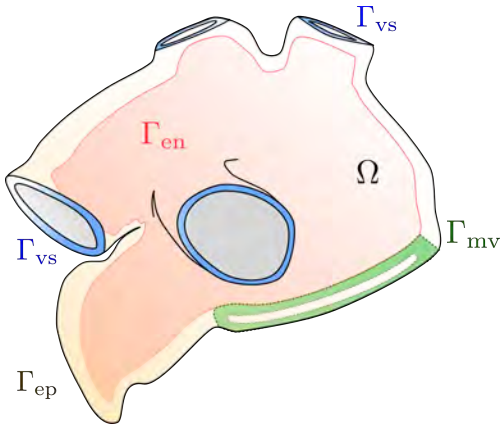

Fig. 1: Geometrical description of the left atrium.

where $\boldsymbol{\Sigma}_{\text{p}}$ accounts for the passive stress behavior of the myocardium and $\boldsymbol{\Sigma}_{\text{a}}$ denotes the active stress.

The passive response is modeled as a combination of hyperelastic and viscous contributions, formulated as

$$\boldsymbol{\Sigma}_{\text{p}} \stackrel{\text{def}}{=} \frac{\partial W_{\text{e}}}{\partial \boldsymbol{E}} + \frac{\partial W_{\text{v}}}{\partial \dot{\boldsymbol{E}}},$$

where $\boldsymbol{E} \stackrel{\text{def}}{=} \frac{1}{2}(\boldsymbol{C} - \mathbb{I})$ stands for the Green–Lagrange strain tensor (with $\mathbb{I}$ denoting the identity matrix in $\mathbb{R}^{3\times 3}$), $\dot{\boldsymbol{E}} \stackrel{\text{def}}{=} \partial_t \boldsymbol{E}$ and W_{e} and W_{v} are the hyperelastic potential and the viscous pseudo-potential, respectively. The myocardium is assumed to be a nearly incompressible, transversely isotropic material with a preferred direction aligned with the local fiber orientation, represented by unit tangent field $\boldsymbol{f}$. Following previous studies on atrial mechanics [34, 37, 52], we consider the Demiray-Gasser strain-energy density function [53, 54]

$$W_{\text{e}} \stackrel{\text{def}}{=} \frac{a_{\text{p}}}{2b_{\text{p}}}\left(e^{b_{\text{p}}(J_1-3)} - 1\right) + \frac{a_{\text{f}}}{2b_{\text{f}}}\left(e^{b_{\text{f}}(J_4-1)^2} - 1\right) + \kappa \log^2 J, \tag{1}$$

where $a_{\text{p}}, b_{\text{p}}, a_{\text{f}}, b_{\text{f}}, \kappa > 0$ are given constitutive parameters. The strain energy depends on the reduced invariants $J_1 \stackrel{\text{def}}{=} J^{-2/3}\,\text{tr}\boldsymbol{C}$ and $J_4 \stackrel{\text{def}}{=} J^{-2/3}\,\boldsymbol{f}^{\top}\boldsymbol{C}\boldsymbol{f}$. The viscous behavior is described through the pseudo-potential

$$W_{\text{v}} \stackrel{\text{def}}{=} \frac{\nu}{2}\,\dot{\boldsymbol{E}} : \dot{\boldsymbol{E}},$$

where $\nu > 0$ denotes the passive viscosity coefficient.

The active behavior is modeled by the multiscale approach outlined in [23, 55]. The contractile response arises from chemical processes in myocytes that induce sarcomere contraction and relaxion, producing the subsequent deformation of the myocardial

tissue along the fibers. This microscopic deformation induces a change in the fiber extension e_c, which drives both the active tension τ_c and the active stiffness k_c of the sarcomeres. The dynamics of these contractile quantities are described by the following extension of the model originally proposed in [56]:

$$\begin{cases} \dot{k}_c = -\big(|u_e| + \alpha_d|\dot{e}_c|\big)k_c + n_0(e_c)k_0\,|u_e|_+ & \text{in} \quad \Omega, \\ \dot{\tau}_c = -\big(|u_e| + \alpha_d|\dot{e}_c|\big)\tau_c + k_c\,\dot{e}_c + n_0(e_c)\sigma_0\,|u_e|_+ & \text{in} \quad \Omega, \end{cases}$$

where k_0 and σ_0 respectively denote the maximum stiffness and contractility. The term $\alpha_d\,|\dot{e}_c|$ accounts for the bridges destruction upon rapid length changes. The parameter $0 \leq n_0(e_c) \leq 1$ is a reduction factor that accounts for the Frank-Starling effect, which relates the force-generating capacity of the cardiac tissue based on its degree of stretch. Finally, $|x|_+ \stackrel{\text{def}}{=} \max\{x, 0\}$ and u_e represents the chemical activation. This source term is modeled phenomenologically as an affine function of the tissue transmembrane potential V_m:

$$u_e = \alpha V_m + \beta \quad \text{in} \quad \Omega, \tag{2}$$

where α and β are given constants (see, e.g., [20]). The transmembrane potential V_m is obtained from the bidomain model of cardiac electrophysiology (see Appendix A).

The contractile and elastic stresses within the sarcomeres are respectively given by

$$\sigma_c = \tau_c + \mu_c\,\dot{e}_c, \tag{3}$$

and

$$\sigma_s = E_s\,e_s, \tag{4}$$

where $\mu_c > 0$ is the viscous dissipation parameter and e_s for the elastic extension of the sarcomeres, while E_s denotes the elastic modulus of the passive sarcomere response. The total stress along the fibers, denoted by σ_a, can be expressed in terms of contractile and elastic stresses via the relation (see [23])

$$\sigma_a = \frac{\sigma_c}{1 + 2e_s} = \frac{\sigma_s}{1 + 2e_c}. \tag{5}$$

Furthermore, the total fiber extension $e_f \stackrel{\text{def}}{=} \boldsymbol{f}^T\boldsymbol{E}\boldsymbol{f}$ satisfies

$$1 + 2e_f = (1 + 2e_s)(1 + 2e_c)\,. \tag{6}$$

From (5) and (6), the macroscopic active stress can be written as

$$\sigma_a = E_s\,\frac{e_f - e_c}{(1 + 2e_c)^2}. \tag{7}$$

By combining (3) and (5) with (7), the evolution of the contractile extension e_c is given by the relation

$$\mu_c\dot{e}_c + \tau_c = E_s\,\frac{(e_f - e_c)(1 + 2e_f)}{(1 + 2e_c)^3}. \tag{8}$$

Finally, the active part of the second Piola–Kirchhoff stress tensor is expressed as

$$\boldsymbol{\Sigma}_{\mathrm{a}} = \sigma_{\mathrm{a}} \boldsymbol{f} \otimes \boldsymbol{f} = \frac{E_{\mathrm{s}}\big(\boldsymbol{f}^{\mathrm{T}} \boldsymbol{E} \boldsymbol{f} - e_{\mathrm{c}}\big)}{(1+2e_{\mathrm{c}})^2}\, \boldsymbol{f} \otimes \boldsymbol{f}. \tag{9}$$

Considering the standard 3D space of admissible solid displacements

$$\boldsymbol{V} \stackrel{\mathrm{def}}{=} \left\{ \boldsymbol{v} \in [H^1(\Omega)]^3 : \ \boldsymbol{v}|_{\Gamma_{\mathrm{vs}}} = \boldsymbol{0} \right\}, \tag{10}$$

the weak form of the resulting full 3D electromechanical model of the left atrium reads: For $t > 0$, find the displacements $\boldsymbol{y}(t) \in \boldsymbol{V}$, with $\dot{\boldsymbol{y}} = \partial_t \boldsymbol{y}$, the extension along the fibers $e_{\mathrm{c}} : \Omega \times \mathbb{R}^+ \to \mathbb{R}$, the active stiffness $k_{\mathrm{c}} : \Omega \times \mathbb{R}^+ \to \mathbb{R}^+$ and the active tension $\tau_{\mathrm{c}} : \Omega \times \mathbb{R}^+ \to \mathbb{R}$ such that

$$\begin{cases} \rho \displaystyle\int_\Omega \partial_t \dot{\boldsymbol{y}} \cdot \boldsymbol{v} + \int_\Omega \boldsymbol{\Sigma} : D_{\boldsymbol{y}} \boldsymbol{E} \cdot \boldsymbol{v} + \int_{\Gamma_{\mathrm{mv}}} \big(a\boldsymbol{y} + b\dot{\boldsymbol{y}}\big) \cdot \boldsymbol{v} = -\int_{\Gamma_{\mathrm{en}}} p_{\mathrm{la}} J \boldsymbol{F}^{-\top} \boldsymbol{n} \cdot \boldsymbol{v}, \\ \mu_{\mathrm{c}} \dot{e}_{\mathrm{c}} + \tau_{\mathrm{c}} = E_{\mathrm{s}} \dfrac{(\boldsymbol{f}^\top \boldsymbol{E} \boldsymbol{f} - e_{\mathrm{c}})(1 + 2\boldsymbol{f}^\top \boldsymbol{E} \boldsymbol{f})}{(1+2e_{\mathrm{c}})^3} \quad \text{in} \quad \Omega, \\ \dot{k}_{\mathrm{c}} = -\left(|u_{\mathrm{e}}| + \alpha_{\mathrm{d}} \left|\dot{e}_c\right|\right) k_{\mathrm{c}} + n_0(e_{\mathrm{c}}) k_0 |u_{\mathrm{e}}|_+ \quad \text{in} \quad \Omega, \\ \dot{\tau}_{\mathrm{c}} = -\left(|u_{\mathrm{e}}| + \alpha_{\mathrm{d}} \left|\dot{e}_{\mathrm{c}}\right|\right) \tau_{\mathrm{c}} + \dot{e}_{\mathrm{c}} k_{\mathrm{c}} + n_0(e_{\mathrm{c}}) \sigma_0 |u_{\mathrm{e}}|_+ \quad \text{in} \quad \Omega \end{cases} \tag{11}$$

for all $\boldsymbol{v} \in \boldsymbol{V}$ and where $\rho > 0$ denotes the volumic mass of the atrial wall. Note that the annuli of the pulmonary veins inlets Γ_{vs} are assumed to be fixed and a viscoelastic boundary condition is enforced on the the mitral valve annulus Γ_{mv}. The dynamics of the unknown internal pressure p_{la} in the atrial cavity will be described in Section 2.1.2 below using a lumped parameter modeling.

2.1.1 3D-shell modeling of the left atrium

A fundamental drawback of $(11)_1$ is that due to the intrinsic thin-walled nature of Ω, standard 3D finite element discretizations are prone to become highly sensitive to wall thickness, leading to well-known robustness issues. In particular, the resulting solutions exhibit artificial stiffening effects (see, e.g., [47]). Accurate results typically require substantial mesh refinement, which leads to a significantly more expensive computational problem. These numerical difficulties can be mitigated by adopting reduced kinematic formulations based on shell theory. When combined with appropriate numerical techniques to alleviate locking at the discrete level (see, e.g., [47, 48]), shell formulations considerably reduce the sensitivity of the method to wall thickness and provide a robust alternative to full 3D discretizations. In this work, we consider a thin-wall modeling of the left atrium by building on the reduced 3D-shell model proposed in [48], which consists of approximating the 3D displacement field by a quadratic expansion across the thickness, without requiring a plane-stress assumption (in contrast to standard shell formulations). As demonstrated in [48], this approach yields a well-posed shell model and is asymptotically consistent with classical shell theories in the vanishing-thickness limit.

In what follows, the mid-surface $\mathcal{S}$ of the atrial wall Ω is assumed to be parametrized by a smooth mapping $\boldsymbol{\phi} : \omega \subset \mathbb{R}^2 \to \mathbb{R}^3$, such that $\mathcal{S} = \boldsymbol{\phi}(\omega)$, with $(\xi^1, \xi^2) \in \omega$ denoting the curvilinear coordinates in the reference 2D domain ω. The local geometry of $\mathcal{S}$ is characterized by its covariant basis vectors

$$\boldsymbol{a}_i \stackrel{\text{def}}{=} \partial_{\xi^i} \boldsymbol{\phi} \quad i = 1, 2,$$

which span the tangent plane to the mid-surface $\mathcal{S}$. Consequently, the unit normal vector field $\boldsymbol{a}_3$ is defined as

$$\boldsymbol{a}_3 \stackrel{\text{def}}{=} \frac{\boldsymbol{a}_1 \times \boldsymbol{a}_2}{\|\boldsymbol{a}_1 \times \boldsymbol{a}_2\|}.$$

The reference configuration of the left atrium Ω is finally assumed to be parametrized as

$$\Omega = \boldsymbol{\Phi}\big(\omega \times (-1, 1)\big),$$

with the mapping $\boldsymbol{\Phi} : \omega \times (-1, 1) \to \mathbb{R}^3$ given by the relation

$$\boldsymbol{\Phi}(\xi^1, \xi^2, \xi^3) \stackrel{\text{def}}{=} \boldsymbol{\phi}(\xi^1, \xi^2) + \xi^3 \, \frac{\epsilon(\xi^1, \xi^2)}{2} \, \boldsymbol{a}_3(\xi^1, \xi^2), \tag{12}$$

where ξ^3 denotes the curvilinear coordinate oriented along the unit normal to $\mathcal{S}$, and $\epsilon : \omega \to \mathbb{R}^+$ represents the spatially varying wall thickness. A schematic representation of the mapping $\boldsymbol{\Phi}$ is provided in Fig. 2.

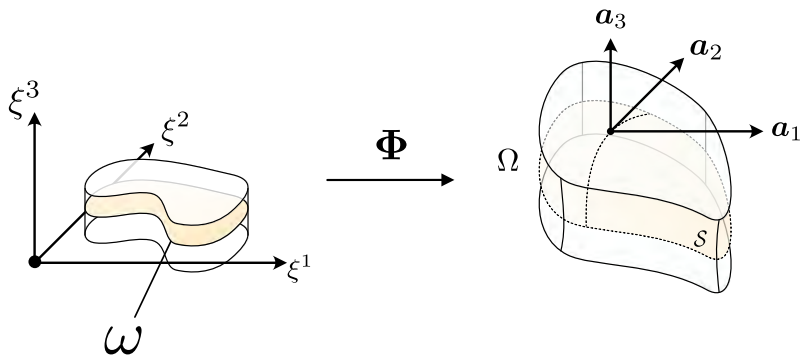

Fig. 2: The geometrical mapping Φ.

The covariant basis vectors describing the full atrial wall geometry are given by $\boldsymbol{g}_i \stackrel{\text{def}}{=} \partial_{\xi^i} \boldsymbol{\Phi}$ with $i = 1, 2, 3$. Finally, the components of the 3D metric tensor in the reference configuration are given by $G_{ij} \stackrel{\text{def}}{=} \boldsymbol{g}_i \cdot \boldsymbol{g}_j$. The corresponding contravariant basis vectors $\boldsymbol{g}^i$ are defined through the orthogonality condition $\boldsymbol{g}^i \cdot \boldsymbol{g}_j = \delta^i_j$, yielding the contravariant metric components $G^{ij} \stackrel{\text{def}}{=} \boldsymbol{g}^i \cdot \boldsymbol{g}^j$.

The fundamental idea for the 3D-shell modeling of the left atrium consists in performing a Galerkin projection of the variational formulation $(11)_1$ by considering the following reduced space (see [48]):

$$\boldsymbol{V}^{\mathrm{sh}} \overset{\mathrm{def}}{=} \left\{ \boldsymbol{v}_{\mathrm{s}} \in \boldsymbol{v} \,:\, \boldsymbol{v} = \boldsymbol{v}_0 + \boldsymbol{v}_1 \xi^3 + \boldsymbol{v}_2 (\xi^3)^2, \quad \boldsymbol{v}_i \in \left[H^1(\mathcal{S}) \right]^3, \quad i = 0, 1, 2 \right\}, \tag{13}$$

where ξ^3 denotes the transverse coordinate introduced in (12) through the geometric mapping $\boldsymbol{\Phi}$. Note that the vector fields $\boldsymbol{v}_i$, $i = 0, 1, 2$, are defined solely on the mid-surface $\mathcal{S}$ and therefore depend only on the tangential coordinates ξ^1 and ξ^2. Therefore, after appropriate composition with the mappings $\boldsymbol{\Phi}$ and $\boldsymbol{\phi}$, the virtual displacement identity in (13) should be read as

$$\boldsymbol{v}(\xi^1, \xi^2, \xi^3) = \boldsymbol{v}_0(\xi^1, \xi^2) + \boldsymbol{v}_1(\xi^1, \xi^2)\xi^3 + \boldsymbol{v}_2(\xi^1, \xi^2)(\xi^3)^2$$

for all $(\xi^1, \xi^2) \in \omega$ and $\xi^3 \in (-1, 1)$.

The proposed 3D-shell model of the left atrium reads therefore as follows:

$$\begin{cases} \text{For } t > 0, \text{ find } \boldsymbol{y}(t) \in \boldsymbol{V}^{\mathrm{sh}}, \text{ with } \dot{\boldsymbol{y}} = \partial_t \boldsymbol{y},\ e_{\mathrm{c}} : \Omega \times \mathbb{R}^+ \to \mathbb{R},\ k_{\mathrm{c}} : \Omega \times \mathbb{R}^+ \to \mathbb{R}^+, \\ \text{and } \tau_{\mathrm{c}} : \Omega \times \mathbb{R}^+ \to \mathbb{R} \text{ such that (11) holds for all } \boldsymbol{v} \in \boldsymbol{V}^{\mathrm{sh}}. \end{cases} \tag{14}$$

It is worth noting that the only difference between this reduced problem and the full 3D formulation of the left atrium presented above lies in the kinematic assumption introduced through the reduced space (13). Additionally, since no plane-stress assumption is imposed in (14), the incorporation of fully 3D, non-quadratic constitutive law (such as the Demiray–Gasser law (1)) is straightforward, in contrast to what occurs with standard shell formulations.

In this framework, the usual mechanical quantities such as the deformation gradient admit a mixed-component representation

$$F^i_j = \delta^i_j + \boldsymbol{g}^i \cdot \boldsymbol{y}_{,j},$$

where $\boldsymbol{y}_{,j}$ denotes the partial derivative of the displacement field with respect to the curvilinear coordinate ξ^j, and the identity term arises from the duality relation $\boldsymbol{g}^i \cdot \boldsymbol{g}_j = \delta^i_j$. Similarly, the covariant components of the Green–Lagrange and right Cauchy-Green strain tensor are respectively given by

$$E_{ij} = \frac{1}{2}(\boldsymbol{y}_{,i} \cdot \boldsymbol{g}_j + \boldsymbol{y}_{,j} \cdot \boldsymbol{g}_i + \boldsymbol{y}_{,i} \cdot \boldsymbol{y}_{,j}), \quad C_{ij} = G_{ij} + \boldsymbol{g}_i \cdot \boldsymbol{y}_{,j} + \boldsymbol{g}_j \cdot \boldsymbol{y}_{,i} + \boldsymbol{y}_{,i} \cdot \boldsymbol{y}_{,j}.$$

2.1.2 0D blood flow modeling in the left cardiac cavities

In order to model the interactions between cavities at a reduced computational cost, while retaining the essential physiological features, we adopt a 0D lumped-parameter description of the circulatory compartments connected to the left atrium. In this framework, each chamber or vascular segment has an associated pressure, while the

flows between compartments are determined through algebraic relations that mimic the effect of valves and vascular resistances.

Blood flow in the left atrium

The exchange of blood between the pulmonary veins, the left atrium and the left ventricle is controlled by the mitral valve, which acts as a unidirectional flow regulator driven by the pressure gradient beetwen the cavities. The valve is considered open when the downstream pressure is lower than the upstream pressure, and closed otherwise. Accordingly, the net flux exiting the left atrium is given by the following expression:

$$Q_{\mathrm{la}} \overset{\mathrm{def}}{=} Q_{\mathrm{vs}}(p_{\mathrm{la}}, p_{\mathrm{vs}}) + Q_{\mathrm{mv}}(p_{\mathrm{la}}, p_{\mathrm{lv}}), \tag{15}$$

with $Q_{\mathrm{vs}}(p_{\mathrm{la}}, p_{\mathrm{vs}}) \overset{\mathrm{def}}{=} k_{\mathrm{vs}}(p_{\mathrm{la}} - p_{\mathrm{vs}})$ and

$$Q_{\mathrm{mv}}\big(p_{\mathrm{lv}}, p_{\mathrm{la}}\big) \overset{\mathrm{def}}{=} \begin{cases} 0 & \text{if} \quad p_{\mathrm{lv}} \geq p_{\mathrm{la}}, \\ k_{\mathrm{mv}}(p_{\mathrm{la}} - p_{\mathrm{lv}}) & \text{if} \quad p_{\mathrm{lv}} < p_{\mathrm{la}}. \end{cases}$$

Here, $p_{\mathrm{vs}}(t)$ and $p_{\mathrm{lv}}(t)$ respectively denote the spatially homogeneous pressures in the pulmonary veins and in the left ventricle, whereas $k_{\mathrm{vs}}, k_{\mathrm{mv}} > 0$ stand for the pulmonary and mitral conductance coefficients. Mass flow in the left atrium is preserved by enforcing the zero net flux condition

$$-\int_{\Gamma_{\mathrm{en}} \cup \Gamma_{\mathrm{mc}}} J\dot{\boldsymbol{y}} \cdot \boldsymbol{F}^{-\top}\boldsymbol{n} + Q_{\mathrm{la}}\big(p_{\mathrm{vs}}, p_{\mathrm{lv}}, p_{\mathrm{la}}\big) = 0,$$

where Γ_{mc} stands for an *ad hoc* surface closure of the mitral valve. Note that, this introduces a scalar constraint in the weak formulation $(14)_1$, with the atrial pressure $p_{\mathrm{la}}(t)$ acting as Lagrange multiplier. In this work, the pulmonary venous pressure $p_{\mathrm{v}}(t)$ is assumed to be given, while the dynamics of p_{lv} are described in the next paragraph using a 0D electromechanical model of the left ventricle.

Reduced electromechanical model of the left ventricle

To capture the hemodynamic coupling between the left atrium and the left ventricle, the ventricular pressure p_{lv} is described using the 0D reduced-order model proposed in [50]. This formulation provides a consistent reduction of the full 3D electromechanical problem (11) proposed in [23] and is adapted to an idealized geometry. The reduced model assumes spherical symmetry for both the geometry and the constitutive behavior. Under this hypothesis, the ventricle is represented as a spherical shell defined by a radius R_0 and wall thickness d_0 in the stress-free reference configuration Ω_{lv}. Therefore, the associated displacement field of the left ventricle $\boldsymbol{y}^{\mathrm{lv}}(t) \overset{\mathrm{def}}{=} y^{\mathrm{lv}}\boldsymbol{i}_r = (R - R_0)\boldsymbol{i}_r$, is restricted to the radial direction $\boldsymbol{i}_r$, where R denotes the current radius.

The myocardium is modeled as an incompressible material, enforcing the isochoric constraint $J = 1$. The stress on the idealized sphere can be represented by an effective spherical stress Σ_{sph}. This term arises from projecting the full stress tensor onto the

reduced radial kinematics (see [50] for derivation details) and incorporates active, passive, and viscous contributions such that

$$\Sigma_{\text{sph}} = \sigma_{\text{a}}^{\text{lv}} + 4(1 - C^{-3}) \left(\frac{\partial W_{\text{e}}^{\text{lv}}}{\partial J_1} + C \frac{\partial W_{\text{e}}^{\text{lv}}}{\partial J_2} \right) + 2 \frac{\partial W_{\text{e}}^{\text{lv}}}{\partial J_4} + \eta \dot{C}(1 + 2C^{-6}).$$

Here, $C \overset{\text{def}}{=} (1+y/R_0)^2$ is the squared circumferential stretch, and J_1,J_2, and J_4 denote the standard reduced invariants of the right Cauchy-Green deformation tensor, with $J_2 \overset{\text{def}}{=} \frac{1}{2}((\text{tr}\boldsymbol{C}^{\text{lv}})^2 - \text{tr}(\boldsymbol{C}^{\text{lv}})^2)J^{-4/3}$, where the right Cauchy-Green deformation tensor of the reduced sphere is defined by

$$\boldsymbol{C}^{\text{lv}} \overset{\text{def}}{=} \begin{pmatrix} C_{\text{rr}} & 0 & 0 \\ 0 & C & 0 \\ 0 & 0 & C \end{pmatrix},$$

with $C_{\text{rr}} \overset{\text{def}}{=} C^{-2}$. The active contribution of the reduced sphere $\sigma_{\text{a}}^{\text{lv}}$ is defined similarly to the atrial tissue in (7) but assuming a circumferential fiber orientation aligned with the orthoradial direction $\boldsymbol{i}_{\phi_1}$ of the sphere, such that $\boldsymbol{f}^{\text{lv}} = \boldsymbol{i}_{\phi_1}$. This results in the following strain along the fibers $e_{\text{f}}^{\text{lv}} \overset{\text{def}}{=} (\boldsymbol{f}^{\text{lv}})^{\top} \boldsymbol{E}^{\text{lv}} \boldsymbol{f}^{\text{lv}}$, where $\boldsymbol{E}^{\text{lv}} \overset{\text{def}}{=} 1/2(\boldsymbol{C}^{\text{lv}} - \mathbb{I})$ represents the Green-Lagrange strain tensor of the reduced sphere.

Although the general expression for Σ_{sph} admits a dependence on the second invariant J_2, the specific strain-energy density function W_{e} adopted in this work for the left ventricle relies exclusively on the isotropic invariant J_1 and the anisotropic invariant J_4. Therefore, following the formulation proposed in [50] and inspired from [57], the elastic potential is defined as

$$W_{\text{e}}^{\text{lv}} = C_0 \exp C_1 (J_1 - 3)^2 + C_2 \exp C_3 (J_4 - 1)^2.$$

The parameters C_0, C_1, C_2 and C_3 are selected to reproduce a physiological response of the left ventricle.

Given the geometrical and kinematical assumptions, the terms of the dynamic balance equation (analogous to $(11)_1$) integrated over the reference domain are space-wise. After some algebraic manipulations, the complete 0D electromechanical formulation for the left ventricle read as follows: Find the radial displacement $y^{\text{lv}} : \mathbb{R}^+ \to \mathbb{R}$, the extension along the fibers $e_{\text{c}}^{\text{lv}} : \mathbb{R}^+ \to \mathbb{R}$, the active stiffness $k_{\text{c}}^{\text{lv}} : \mathbb{R}^+ \to \mathbb{R}^+$, the active tension $\tau_{\text{c}}^{\text{lv}} : \mathbb{R}^+ \to \mathbb{R}$ and the internal pressure $p_{\text{lv}} : \mathbb{R}^+ \to \mathbb{R}$, such that

$$
\begin{cases}
\rho d_0 \ddot{y}^{\mathrm{lv}} + \dfrac{d_0}{R_0}\left(1+\dfrac{y^{\mathrm{lv}}}{R_0}\right)\Sigma_{\mathrm{sph}} = p_{\mathrm{lv}}\left(1+\dfrac{y^{\mathrm{lv}}}{R_0}\right)^2, \\
\Sigma_{\mathrm{sph}} = \sigma_{\mathrm{a}}^{\mathrm{lv}} + 4(1-C^{-3})\left(\dfrac{\partial W_{\mathrm{e}}^{\mathrm{lv}}}{\partial J_1} + C\dfrac{\partial W_{\mathrm{e}}^{\mathrm{lv}}}{\partial J_2}\right) + 2\dfrac{\partial W_{\mathrm{e}}^{\mathrm{lv}}}{\partial J_4} + 2\eta\dot{C}(1-2C^{-6}), \\
\sigma_{\mathrm{a}}^{\mathrm{lv}} = E_{\mathrm{s}}^{\mathrm{lv}}\dfrac{e_{\mathrm{f}}^{\mathrm{lv}} - e_{\mathrm{c}}^{\mathrm{lv}}}{(1+2e_{\mathrm{c}}^{\mathrm{lv}})}, \\
\tau_{\mathrm{c}}^{\mathrm{lv}} + \mu^{\mathrm{lv}}\dot{e}_{\mathrm{c}}^{\mathrm{lv}} = E_{\mathrm{s}}\dfrac{(e_{\mathrm{f}}^{\mathrm{lv}} - e_{\mathrm{c}}^{\mathrm{lv}})(1+2e_{\mathrm{f}}^{\mathrm{lv}})}{(1+2e_{\mathrm{c}}^{\mathrm{lv}})^3}, \\
\dot{k}_{\mathrm{c}}^{\mathrm{lv}} = -\left(|u_{\mathrm{e}}^{\mathrm{lv}}| + \alpha_{\mathrm{d}}^{\mathrm{lv}}|\dot{e}_{\mathrm{c}}^{\mathrm{lv}}|\right)k_{\mathrm{c}}^{\mathrm{lv}} + n_0(e_{\mathrm{c}}^{\mathrm{lv}})k_0^{\mathrm{lv}}|u_{\mathrm{e}}^{\mathrm{lv}}|_+, \\
\dot{\tau}_{\mathrm{c}}^{\mathrm{lv}} = -\left(|u_{\mathrm{e}}^{\mathrm{lv}}| + \alpha_{\mathrm{d}}^{\mathrm{lv}}|\dot{e}_{\mathrm{c}}^{\mathrm{lv}}|\right)\tau_{\mathrm{c}}^{\mathrm{lv}} + n_0(e_{\mathrm{c}}^{\mathrm{lv}})\sigma_0^{\mathrm{lv}}|u_{\mathrm{e}}^{\mathrm{lv}}|_+ + k_{\mathrm{c}}^{\mathrm{lv}}\dot{e}_{\mathrm{c}}^{\mathrm{lv}}.
\end{cases}
\tag{16}
$$

In this formulation, all variables marked with the superscript $^{\mathrm{lv}}$ denote quantities specific to the reduced-order electromechanical model of the left ventricle.

Blood flow in the left ventricle

Blood flow in the left ventricle is regulated by the coordinated action of the mitral and aortic valves. Depending on the cardiac phase, namely, filling, isovolumetric contraction, ejection, or isovolumetric relaxation, the status of these valves (mitral-aortic) transitions sequentially: open-closed, closed-closed, closed-open, and closed-closed, respectively. Consequently, the total flux on the left ventricle, Q_{lv} can be modeled as

$$
Q_{\mathrm{lv}}(p_{\mathrm{lv}}, p_{\mathrm{ar}}, p_{\mathrm{la}}) \overset{\mathrm{def}}{=} \begin{cases} -Q_{\mathrm{mv}}(p_{\mathrm{la}}, p_{\mathrm{lv}}) & \text{if} \quad p_{\mathrm{lv}} \le p_{\mathrm{la}}, \\ 0 & \text{if} \quad p_{\mathrm{la}} \le p_{\mathrm{lv}} \le p_{\mathrm{ar}}, \\ k_{\mathrm{ar}}(p_{\mathrm{lv}} - p_{\mathrm{ar}}) & \text{if} \quad p_{\mathrm{lv}} \ge p_{\mathrm{ar}}, \end{cases}
\tag{17}
$$

where $k_{\mathrm{ar}} > 0$ is the arterialconductance, while p_{ar} denotes the pressure in the aorta.

Mass conservation requires that the net flux entering or leaving the left ventricle balances the rate of volume change of the cavity. Expressed in terms of spherical shell kinematics, this dynamic continuity equation is defined as

$$
\dot{V} = 4\pi R_0^2\left(1+\frac{y^{\mathrm{lv}}}{R_0}\right)^2 \dot{y}^{\mathrm{lv}} = -Q_{\mathrm{lv}}(p_{\mathrm{lv}}, p_{\mathrm{ar}}, p_{\mathrm{la}}).
$$

The aortic pressure p_{ar} is determined using a lumped-parameter model that describes the systemic circulation downstream of the left ventricle. Specifically, we employ the two-element Windkessel model (see, e.g., [58]), which characterizes the external

circulatory dynamics as

$$\begin{cases} C_{\mathrm{p}}\dot{p}_{\mathrm{ar}} + \dfrac{p_{\mathrm{ar}} - p_{\mathrm{lv}}}{R_{\mathrm{p}}} = |Q_{\mathrm{lv}}(p_{\mathrm{lv}}, p_{\mathrm{ar}}, p_{\mathrm{la}})|_+, \\ C_{\mathrm{d}}\dot{p}_{\mathrm{d}} + \dfrac{p_{\mathrm{d}} - p_{\mathrm{ar}}}{R_{\mathrm{p}}} = \dfrac{p_{\mathrm{v}} - p_{\mathrm{d}}}{R_{\mathrm{d}}}. \end{cases} \tag{18}$$

where C_{p} and C_{d} denote the proximal and distal compliances, respectively, while R_{p} and R_{d} correspond to the proximal and distal resistances. The symbols p_{v} and p_{d} represent the venous and distal pressures, respectively.

2.1.3 Complete mathematical model

The complete formulation of the proposed 3D-shell electromechanical model of the left atrium read as follows: For $t > 0$, find $\boldsymbol{y}(t) \in \boldsymbol{V}^{\mathrm{sh}}$, with $\dot{\boldsymbol{y}} = \partial_t \boldsymbol{y}$, $e_{\mathrm{c}} : \Omega \times \mathbb{R}^+ \to \mathbb{R}$, $k_{\mathrm{c}} : \Omega \times \mathbb{R}^+ \to \mathbb{R}^+$, $\tau_{\mathrm{c}} : \Omega \times \mathbb{R}^+ \to \mathbb{R}$, $p_{\mathrm{at}} : \mathbb{R}^+ \to \mathbb{R}$, $y^{\mathrm{lv}} : \mathbb{R}^+ \to \mathbb{R}$, $e_{\mathrm{c}}^{\mathrm{lv}} : \mathbb{R}^+ \to \mathbb{R}$, $k_{\mathrm{c}}^{\mathrm{lv}} : \mathbb{R}^+ \to \mathbb{R}^+$, $\tau_{\mathrm{c}}^{\mathrm{lv}} : \mathbb{R}^+ \to \mathbb{R}$ and $p_{\mathrm{lv}} : \mathbb{R}^+ \to \mathbb{R}$, such that

$$\begin{cases} \rho \displaystyle\int_\Omega \partial_t \dot{\boldsymbol{y}} \cdot \boldsymbol{v} + \int_\Omega \boldsymbol{\Sigma} : D_{\boldsymbol{y}} \boldsymbol{E} \cdot \boldsymbol{v} + \int_{\Gamma_{\mathrm{mv}}} \big(a\boldsymbol{y} + b\dot{\boldsymbol{y}}\big) \cdot \boldsymbol{v} = -\int_{\Gamma_{\mathrm{en}}} p_{\mathrm{la}} J \boldsymbol{F}^{-\top} \boldsymbol{n} \cdot \boldsymbol{v} \quad \forall \boldsymbol{v} \in \boldsymbol{V}^{\mathrm{sh}}, \\ \mu_{\mathrm{c}} \dot{e}_{\mathrm{c}} + \tau_{\mathrm{c}} = E_{\mathrm{s}} \dfrac{(\boldsymbol{f}^\top \boldsymbol{E} \boldsymbol{f} - e_{\mathrm{c}})(1 + 2\boldsymbol{f}^\top \boldsymbol{E} \boldsymbol{f})}{(1 + 2e_{\mathrm{c}})^3} \quad \text{in} \quad \Omega, \\ \dot{k}_{\mathrm{c}} = -\left(|u_{\mathrm{e}}| + \alpha_{\mathrm{d}} \, |\dot{e}_c|\right) k_{\mathrm{c}} + n_0(e_{\mathrm{c}}) k_0 |u_{\mathrm{e}}|_+ \quad \text{in} \quad \Omega, \\ \dot{\tau}_{\mathrm{c}} = -\left(|u_{\mathrm{e}}| + \alpha_{\mathrm{d}} \, |\dot{e}_{\mathrm{c}}|\right) \tau_{\mathrm{c}} + \dot{e}_{\mathrm{c}} k_{\mathrm{c}} + n_0(e_{\mathrm{c}}) \sigma_0 |u_{\mathrm{e}}|_+ \quad \text{in} \quad \Omega, \\ -\displaystyle\int_{\Gamma_{\mathrm{en}} \cup \Gamma_{\mathrm{mc}}} J \dot{\boldsymbol{y}} \cdot \boldsymbol{F}^{-\top} \boldsymbol{n} + Q\big(p_{\mathrm{vs}}, p_{\mathrm{lv}}, p_{\mathrm{la}}\big) = 0, \\ \rho d_0 \ddot{y}^{\mathrm{lv}} + \dfrac{d_0}{R_0}\left(1 + \dfrac{y^{\mathrm{lv}}}{R_0}\right) \Sigma_{\mathrm{sph}} = p_{\mathrm{lv}} \left(1 + \dfrac{y^{\mathrm{lv}}}{R_0}\right)^2, \\ \sigma_{\mathrm{a}}^{\mathrm{lv}} = E_{\mathrm{s}}^{\mathrm{lv}} \dfrac{e_{\mathrm{f}}^{\mathrm{lv}} - e_{\mathrm{c}}^{\mathrm{lv}}}{(1 + 2e_{\mathrm{c}}^{\mathrm{lv}})}, \\ \tau_{\mathrm{c}}^{\mathrm{lv}} + \mu^{\mathrm{lv}} \dot{e}_{\mathrm{c}}^{\mathrm{lv}} = E_{\mathrm{s}}^{\mathrm{lv}} \dfrac{(e_{\mathrm{f}}^{\mathrm{lv}} - e_{\mathrm{c}}^{\mathrm{lv}})(1 + 2e_{\mathrm{f}}^{\mathrm{lv}})}{(1 + 2e_{\mathrm{c}}^{\mathrm{lv}})^3}, \\ \dot{k}_{\mathrm{c}}^{\mathrm{lv}} = -\left(|u_{\mathrm{e}}^{\mathrm{lv}}| + \alpha_{\mathrm{d}}^{\mathrm{lv}} |\dot{e}_{\mathrm{c}}^{\mathrm{lv}}|\right) k_{\mathrm{c}}^{\mathrm{lv}} + n_0(e_{\mathrm{c}}^{\mathrm{lv}}) k_0^{\mathrm{lv}} |u_{\mathrm{e}}^{\mathrm{lv}}|_+, \\ \dot{\tau}_{\mathrm{c}}^{\mathrm{lv}} = -\left(|u_{\mathrm{e}}^{\mathrm{lv}}| + \alpha_{\mathrm{d}}^{\mathrm{lv}} |\dot{e}_{\mathrm{c}}^{\mathrm{lv}}|\right) \tau_{\mathrm{c}}^{\mathrm{lv}} + n_0(e_{\mathrm{c}}^{\mathrm{lv}}) \sigma_0^{\mathrm{lv}} |u_{\mathrm{e}}^{\mathrm{lv}}|_+ + k_{\mathrm{c}}^{\mathrm{lv}} \dot{e}_{\mathrm{c}}^{\mathrm{lv}}, \\ 4\pi R_0^2 \left(1 + \dfrac{y^{\mathrm{lv}}}{R_0}\right)^2 \dot{y}^{\mathrm{lv}} + Q_{\mathrm{lv}}(p_{\mathrm{lv}}, p_{\mathrm{ar}}, p_{\mathrm{la}}) = 0, \\ C_{\mathrm{p}}\dot{p}_{\mathrm{ar}} + \dfrac{p_{\mathrm{ar}} - p_{\mathrm{lv}}}{R_{\mathrm{p}}} = |Q_{\mathrm{lv}}(p_{\mathrm{lv}}, p_{\mathrm{ar}}, p_{\mathrm{la}})|_+, \\ C_{\mathrm{d}}\dot{p}_{\mathrm{d}} + \dfrac{p_{\mathrm{d}} - p_{\mathrm{ar}}}{R_{\mathrm{p}}} = \dfrac{p_{\mathrm{v}} - p_{\mathrm{d}}}{R_{\mathrm{d}}}. \end{cases} \tag{19}$$

This geometrically heterogeneous coupled non-linear system is schematically illustrated in Fig. 3.

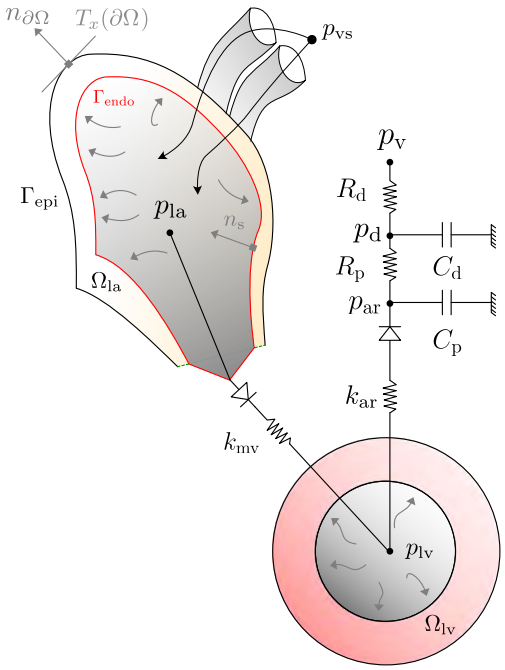

Fig. 3: Illustration of the different components involved in the 3D-shell model of the left atrium (19).

2.2 Numerical approximation

In this section, we detail the numerical approximation of the coupled electromechanical model (19). We first present the time semi-discrete formulation, using a modified midpoint scheme for the mechanical and hemodynamic equations, together with a backward Euler method for the active variables. We then introduce the spatial discretization of the 3D-shell atrial problem using $\mathbb{P}_1 \otimes \mathbb{P}_2$ prismatic finite elements.

2.2.1 Time discretization

The time interval $(0, T_{\mathrm{f}})$ is partitioned into N sub-intervals (t_n, t_{n+1}), where $t_n \overset{\mathrm{def}}{=} \tau n$, $T_{\mathrm{f}} = t_N$, and $\tau > 0$ denotes the time-step length. In what follows, the following standard notation will be employed:

$$\partial_\tau f^{n+1} \overset{\mathrm{def}}{=} \frac{1}{\tau}(f^{n+1} - f^n), \quad f^{n+\frac{1}{2}} \overset{\mathrm{def}}{=} \frac{f^n + f^{n+1}}{2},$$

for the first backward difference and the midpoint approximation, respectively.

The time discretization of the coupled electromechanical system (19) relies on a mixed mid-point/back-Euler scheme. Specifically, in the spirit of [23], the 3D-shell electromechanical model (14) and the reduced valve relations (15) are discretized in time using a mid-point approximation, while the internal variables governing active contraction are updated using a first-order Backward Euler scheme written in therms of the discrete unknowns

$$e_{\mathrm{c}}^{n+1}, \qquad \varrho^{\,n+1} \stackrel{\mathrm{def}}{=} \tau_{\mathrm{c}}^{n+1}/\sqrt{k_{\mathrm{c}}^{n+1}}, \qquad \gamma^{\,n+1} \stackrel{\mathrm{def}}{=} \sqrt{k_{\mathrm{c}}^{n+1}}. \tag{20}$$

This time discretization yields an energy-preserving scheme (see [23]).

Similarly, for the reduced ventricular model (16), the momentum equation, the valve relations (17), and the circulatory subsystem (18) are discretized using the mid-point approximation. The corresponding active variables $(16)_{4,5,6}$ are directly discretized in time using a first-order Backward Euler approximation. In both systems, the contributions coming from the reduction factor n_0 are treated in a explicit fashion.

Finally, the coupling between the two chambers is discretized in time using staggered explicit scheme. The left-ventricular pressure involved in the volume constraint of 3D-shell atrial formulation is evaluated explicitly as $p_{\mathrm{lv}}^{n-\frac{1}{2}}$, viz.,

$$\int_{\Gamma_{\mathrm{en}}\cup\Gamma_{\mathrm{mc}}} J^{n+\frac{1}{2}}\dot{\boldsymbol{y}}^{n+\frac{1}{2}}\cdot\left(\boldsymbol{F}^{n+\frac{1}{2}}\right)^{-\top}\boldsymbol{n} = Q_{\mathrm{la}}\left(p_{\mathrm{vs}}(t_{n+\frac{1}{2}}), p_{\mathrm{lv}}^{n-\frac{1}{2}}, p_{\mathrm{la}}^{n+\frac{1}{2}}\right),$$

whereas the new atrial pressure p_{la}^{n+1} obtained from the 3D-shell model is used as input for the 0D ventricular model, namely,

$$\begin{cases} 4\pi R_0^2\left(1+\dfrac{y^{\mathrm{lv},\,n+\frac{1}{2}}}{R_0}\right)^2\dot{y}^{\mathrm{lv},\,n+\frac{1}{2}} + Q_{\mathrm{lv}}(p_{\mathrm{lv}}^{n+\frac{1}{2}}, p_{\mathrm{ar}}^{n+\frac{1}{2}}, p_{\mathrm{la}}^{n+\frac{1}{2}}) = 0, \\ C_{\mathrm{p}}\partial_\tau p_{\mathrm{ar}}^{n+1} + \dfrac{p_{\mathrm{ar}}^{n+\frac{1}{2}} - p_{\mathrm{lv}}^{n+\frac{1}{2}}}{R_{\mathrm{p}}} = |Q_{\mathrm{lv}}(p_{\mathrm{lv}}^{n+\frac{1}{2}}, p_{\mathrm{ar}}^{n+\frac{1}{2}}, p_{\mathrm{la}}^{n+\frac{1}{2}})|_+. \end{cases}$$

This staggered solution procedure avoids the computational cost of a fully monolithic approach and has been found numerically stable for all the regimes considered (see Section 3). The resulting time semi-discrete approximation of (19) reads therefore as follows: For $n \geq 0$,

1. 3D-shell atrial electromechanics: Find $(\boldsymbol{y}^{n+1}, \dot{\boldsymbol{y}}^{n+1}, e_{\mathrm{c}}^{n+1}, \varrho^{n+1}, \gamma^{n+1}, p_{\mathrm{la}}^{n+1}) \in \boldsymbol{V}^{\mathrm{sh}} \times \boldsymbol{V}^{\mathrm{sh}} \times \mathbb{R} \times \mathbb{R} \times \mathbb{R}^{+} \times \mathbb{R}$, with $\dot{\boldsymbol{y}}^{n+\frac{1}{2}} = \partial_\tau \boldsymbol{y}^{n+1}$, such that

$$
\begin{cases}
\rho_{\mathrm{s}} \displaystyle\int_\Omega \partial_\tau \dot{\boldsymbol{y}}^{n+1} \cdot \boldsymbol{v} + \int_\Omega \boldsymbol{\Sigma}^{n+\frac{1}{2}} : D_{\boldsymbol{y}} \boldsymbol{E}^{n+\frac{1}{2}} \cdot \boldsymbol{v} + \int_{\Gamma_{\mathrm{mv}}} \left(a \boldsymbol{y}^{n+\frac{1}{2}} + b \dot{\boldsymbol{y}}^{n+\frac{1}{2}} \right) \cdot \boldsymbol{v} \\
\quad = - \displaystyle\int_{\Gamma_{\mathrm{en}}} J^{n+\frac{1}{2}} p_{\mathrm{la}}^{n+\frac{1}{2}} \left(\boldsymbol{F}^{n+\frac{1}{2}} \right)^{-\top} \boldsymbol{n} \cdot \boldsymbol{v} \quad \forall \boldsymbol{v} \in \boldsymbol{V}^{\mathrm{sh}}, \\
\boldsymbol{\Sigma}^{n+\frac{1}{2}} = \boldsymbol{\Sigma}_{\mathrm{p}}^{n+\frac{1}{2}} + \dfrac{E_{\mathrm{s}} \left(\boldsymbol{f}^\top \boldsymbol{E}^{n+\frac{1}{2}} \boldsymbol{f} - e_{\mathrm{c}}^{n+\frac{1}{2}} \right)}{\left(1 + 2 e_{\mathrm{c}}^{n+\frac{1}{2}} \right)^2} \boldsymbol{f} \otimes \boldsymbol{f}, \\
\gamma^{n+1} \varrho^{n+1} + \mu_{\mathrm{c}} \partial_\tau e_{\mathrm{c}}^{n+1} = E_{\mathrm{s}} \dfrac{\left(\boldsymbol{f}^\top \boldsymbol{E}^{n+\frac{1}{2}} \boldsymbol{f} - e_{\mathrm{c}}^{n+\frac{1}{2}} \right) \left(1 + 2 \boldsymbol{f}^\top \boldsymbol{E}^{n+\frac{1}{2}} \boldsymbol{f} \right)}{\left(1 + 2 e_{\mathrm{c}}^{n+\frac{1}{2}} \right)^3}, \\
\partial_\tau (\gamma^{n+1})^2 = - \left(\left| u_{\mathrm{e}}^{n+1} \right| + \alpha_{\mathrm{d}} \left| \partial_\tau e_{\mathrm{c}}^{n+1} \right| \right) (\gamma^{n+1})^2 + n_0(e_{\mathrm{c}}^n) k_0 \left| u_{\mathrm{e}}^{n+1} \right|_+, \\
\partial_\tau \varrho^{n+1} = \gamma^{n+1} \partial_\tau e_{\mathrm{c}}^{n+1} + \dfrac{n_0(e_{\mathrm{c}}^n) \sigma_0 \left| u_{\mathrm{e},l}^{n+1} \right|_+}{\gamma^{n+1}} \left(1 - \dfrac{k_0}{2 \sigma_0 \gamma^{n+1}} \varrho^{n+1} \right) \\
\quad - \dfrac{1}{2} \left(\left| u_{\mathrm{e}}^{n+\frac{1}{2}} \right| + \left| \partial_\tau e_{\mathrm{c}}^{n+1} \right| \right) \varrho^{n+1}, \\
\displaystyle\int_{\Gamma_{\mathrm{en}} \cup \Gamma_{\mathrm{mc}}} J^{n+\frac{1}{2}} \dot{\boldsymbol{y}}^{n+\frac{1}{2}} \cdot \left(\boldsymbol{F}^{n+\frac{1}{2}} \right)^{-\top} \boldsymbol{n} = Q_{\mathrm{la}} \left(p_{\mathrm{vs}}(t_{n+\frac{1}{2}}), p_{\mathrm{lv}}^{n-\frac{1}{2}}, p_{\mathrm{la}}^{n+\frac{1}{2}} \right),
\end{cases}
\tag{21}
$$

2. 0D ventricular electromechanics: Find $\left(y^{\mathrm{lv},n+1}, \dot{y}^{\mathrm{lv},n+1}, e_{\mathrm{c}}^{\mathrm{lv},n+1}, k_{\mathrm{c}}^{\mathrm{lv},n+1}, \tau_{\mathrm{c}}^{\mathrm{lv},n+1}, p_{\mathrm{lv}}^{n+1}\right) \in \mathbb{R}^6$ with $\dot{y}^{\mathrm{lv},n+\frac{1}{2}} = \partial_\tau y^{\mathrm{lv},n+1}$, such that

$$
\begin{cases}
\rho d_0 \partial_\tau \dot{y}^{\mathrm{lv},\,n+1} + \dfrac{d_0}{R_0}\left(1 + \dfrac{y^{\mathrm{lv},\,n+\frac{1}{2}}}{R_0}\right)\Sigma_{\mathrm{sph}}^{n+\frac{1}{2}} = p_{\mathrm{lv}}^{n+\frac{1}{2}}\left(1 + \dfrac{y^{\mathrm{lv},\,n+\frac{1}{2}}}{R_0}\right)^2, \\
\Sigma_{\mathrm{sph}}^{n+\frac{1}{2}} = \sigma_{\mathrm{a}}^{\mathrm{lv},n+\frac{1}{2}} + 4(1-(C^{n+\frac{1}{2}})^{-3})\left(\dfrac{\partial W_{\mathrm{e}}^{\mathrm{lv},\,n+\frac{1}{2}}}{\partial J_1} + C^{n+\frac{1}{2}}\dfrac{\partial W_{\mathrm{e}}^{\mathrm{lv},\,n+\frac{1}{2}}}{\partial J_2}\right) \\
\quad + 2\dfrac{\partial W_{\mathrm{e}}^{\mathrm{lv},\,n+\frac{1}{2}}}{\partial J_4} + 2\eta\dot{C}^{n+\frac{1}{2}}(1-2(C^{n+\frac{1}{2}})^{-6}), \\
\sigma_{\mathrm{a}}^{\mathrm{lv},\,n+\frac{1}{2}} = E_{\mathrm{s}}^{\mathrm{lv}}\dfrac{e_{\mathrm{f}}^{\mathrm{lv},\,n+\frac{1}{2}} - e_{\mathrm{c}}^{\mathrm{lv},\,n+\frac{1}{2}}}{(1+2e_{\mathrm{c}}^{\mathrm{lv},\,n+\frac{1}{2}})}, \\
\tau_{\mathrm{c}}^{\mathrm{lv},\,n+1} + \mu^{\mathrm{lv}}\partial_\tau e_{\mathrm{c}}^{\mathrm{lv},\,n+1} = E_{\mathrm{s}}^{\mathrm{lv}}\dfrac{(e_{\mathrm{f}}^{\mathrm{lv},\,n+1} - e_{\mathrm{c}}^{\mathrm{lv},\,n+1})(1+2e_{\mathrm{f}}^{\mathrm{lv},\,n+1})}{(1+2e_{\mathrm{c}}^{\mathrm{lv},\,n+1})^3}, \\
\partial_\tau k_{\mathrm{c}}^{\mathrm{lv},\,n+1} = -\left(|u_{\mathrm{e}}^{\mathrm{lv}}(t_{n+1})| + \alpha_{\mathrm{d}}^{\mathrm{lv}}|\partial_\tau e_{\mathrm{c}}^{\mathrm{lv},\,n+1}|\right)k_{\mathrm{c}}^{\mathrm{lv},\,n+1} + n_0(e_{\mathrm{c}}^{\mathrm{lv,n}})k_0^{\mathrm{lv}}|u_{\mathrm{e}}^{\mathrm{lv}}(t_{n+1})|_+, \\
\partial_\tau \tau_{\mathrm{c}}^{\mathrm{lv},\,n+1} = -\left(|u_{\mathrm{e}}^{\mathrm{lv}}(t_{n+1})| + \alpha_{\mathrm{d}}^{\mathrm{lv}}|\partial_\tau e_{\mathrm{c}}^{\mathrm{lv},\,n+1}|\right)\tau_{\mathrm{c}}^{\mathrm{lv},\,n+1} + n_0(e_{\mathrm{c}}^{\mathrm{lv,n}})\sigma_0^{\mathrm{lv}}|u_{\mathrm{e}}^{\mathrm{lv}}(t_{n+1})|_+ \\
\quad + k_{\mathrm{c}}^{\mathrm{lv},\,n+1}\dot{e}_{\mathrm{c}}^{\mathrm{lv},\,n+1}, \\
4\pi R_0^2\left(1 + \dfrac{y^{\mathrm{lv},\,n+\frac{1}{2}}}{R_0}\right)^2 \dot{y}^{\mathrm{lv},\,n+\frac{1}{2}} + Q_{\mathrm{lv}}(p_{\mathrm{lv}}^{n+\frac{1}{2}}, p_{\mathrm{ar}}^{n+\frac{1}{2}}, p_{\mathrm{la}}^{n+\frac{1}{2}}) = 0, \\
C_{\mathrm{p}}\partial_\tau p_{\mathrm{ar}}^{n+1} + \dfrac{p_{\mathrm{ar}}^{n+\frac{1}{2}} - p_{\mathrm{lv}}^{n+\frac{1}{2}}}{R_{\mathrm{p}}} = |Q_{\mathrm{lv}}(p_{\mathrm{lv}}^{n+\frac{1}{2}}, p_{\mathrm{ar}}^{n+\frac{1}{2}}, p_{\mathrm{la}}^{n+\frac{1}{2}})|_+, \\
C_{\mathrm{d}}\partial_\tau p_{\mathrm{d}}^{n+1} + \dfrac{p_{\mathrm{d}}^{n+\frac{1}{2}} - p_{\mathrm{ar}}^{n+\frac{1}{2}}}{R_{\mathrm{p}}} = \dfrac{p_{\mathrm{v}}(t_{n+\frac{1}{2}}) - p_{\mathrm{d}}^{n+\frac{1}{2}}}{R_{\mathrm{d}}}.
\end{cases}
\tag{22}
$$

2.2.2 Fully discrete method

Having specified the time discretization and the explicit coupling strategy in (21)-(22), we now introduce the spatial discretization used for the 3D-shell atrial sub-problem (21). The reference domain Ω is discretized using a computational mesh $\mathcal{T}_h$ composed of triangular prismatic elements (see Fig. 4). The construction of this mesh relies on the following geometrical steps:

- An approximation of the atrial mid-surface $\mathcal{S}$, represented by a triangulation $\mathcal{T}_h^{\mathcal{S}}$ made of linear triangles;
- An approximation of the unit normal to $\mathcal{S}$ at each vertex of $\mathcal{T}_h^{\mathcal{S}}$;
- An approximation of the local atrial wall thickness associated with each vertex of $\mathcal{T}_h^{\mathcal{S}}$.

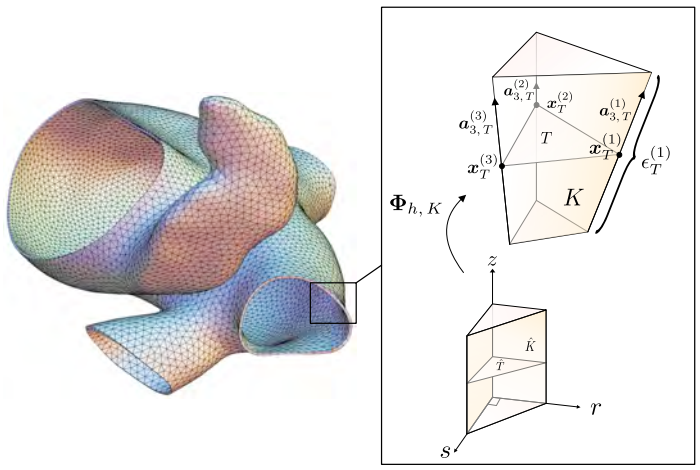

Fig. 4: Left: Prismatic mesh of the left-atrial wall Ω. Right: The map $\Phi_{h,K}$ between the reference and current element of the mesh $\mathcal{T}_h$.

Let $\widehat{K} \overset{\text{def}}{=} \widehat{T} \times (-1, 1)$ be the reference unit prism, where $\widehat{T}$ stands for the reference unit triangle in $\mathbb{R}^2$. Each element K of the computational prismatic mesh $\mathcal{T}_h$ is obtained as the image of the local mapping $\boldsymbol{\Phi}_{h,K} : \widehat{K} \to K \subset \mathbb{R}^3$ defined by

$$\boldsymbol{\Phi}_{h,K}(r,s,z) \overset{\text{def}}{=} \sum_{i=1}^{3} \lambda_i(r,s) \left(\boldsymbol{x}_T^{(i)} + z \frac{\epsilon_K^{(i)}}{2} \boldsymbol{a}_{3,T}^{(i)} \right) \quad \forall (r,s,z) \in \widehat{K}, \tag{23}$$

where $\{\lambda_i\}_{i=1}^3$ stand for the 2D affine shape functions of the reference element $\widehat{T}$, $\{\boldsymbol{x}_T^{(i)}\}_{i=1}^3$ denote the positions of the nodes of the mid-surface triangle $T \in \mathcal{T}_h^{\mathcal{S}}$ associated to the prismatic element $K \in \mathcal{T}_h$ and $\{\boldsymbol{a}_{3,T}^{(i)}\}_{i=1}^3$, $\{\epsilon_T^{(i)}\}_{i=1}^3$ respectively represent the normal vectors to the mid-surface $\mathcal{S}$ and the thickness associated to each node of the triangle T. All these geometrical ingredients are illustrated in Fig. 4.

It is worth noting that the mapping $\boldsymbol{\Phi}_{h,K}$ defined in (23) provides a piecewise parametrization of the computational domain, where (r, s) represent the local coordinates tangential to the mid-surface and z denotes the coordinate in the direction normal to it. This construction can be regarded as the discrete analogue of the continuous mapping (12). However, it offers a practical advantage, instead of requiring an explicit parametrization $\boldsymbol{\phi}$ of the mid-surface $\mathcal{S}$, it only relies on its discrete approximation given by the triangulation $\mathcal{T}_h^{\mathcal{S}}$ together with the nodal normal vectors $\boldsymbol{a}_{3,T}^{(i)}$ and the nodal thickness values $\epsilon_T^{(i)}$.

The 3D-shell electromechanical formulation of the left atrium (21) is spatially discretized using the following finite element approximation of the space $\boldsymbol{V}^{\text{sh}}$:

$$\boldsymbol{V}_h^{\text{sh}} \overset{\text{def}}{=} \left\{ \boldsymbol{v}_h \in \boldsymbol{V} \,:\, \boldsymbol{v}_h \circ \Phi_{h,K} = \sum_{i=1}^{3} \lambda_i(r,s) \left(\boldsymbol{v}_0^{(i)} + \boldsymbol{v}_1^{(i)} z + \boldsymbol{v}_2^{(i)} (z)^2 \right) \quad \forall K \in \mathcal{T}_h, \right.$$

$$\boldsymbol{v}_j^{(i)} \in \mathbb{R}^3, \quad i = 1,2,3, \quad j = 0,1,2 \Big\}, \quad (24)$$

which corresponds to the tensorization of a $\mathbb{P}_1$ approximation in the in-plane coordinates (r, s) with a $\mathbb{P}_2$ approximation along the transverse coordinate z. Therefore, the computer implementation of this 3D-shell element is analogous to that of a standard 3D finite element. The set $\{\boldsymbol{v}_j^{(i)}\}_{j=0,1,2}^{i=1,2,3}$ in (24) represents the 27 degrees of freedom of the displacement in each prismatic element $K \in \mathcal{T}_h$. Furthermore, as outlined in [48], for each $\boldsymbol{v}_h \in \boldsymbol{V}_h^{\mathrm{sh}}$ the following equivalent representation holds

$$\boldsymbol{v}_h \circ \Phi_{h,K} = \sum_{i=1}^{3} \lambda_i(r,s) \left[\frac{(z-1)z}{2} \boldsymbol{v}_{\mathrm{bot}}^{(i)} + (1-(z)^2)\boldsymbol{v}_{\mathrm{mid}}^{(i)} + \frac{(z+1)z}{2} \boldsymbol{v}_{\mathrm{upp}}^{(i)} \right],$$

where the subscripts $_{\mathrm{bot},\mathrm{mid},\mathrm{upp}}$ denote the displacement degrees of freedom associated with the bottom, middle, and upper triangles of the prismatic element (see Fig. 4).

A Mixed Interpolation of Tensorial Components (MITC) technique is employed to treat the transverse strain components, as required in shell formulations to avoid numerical locking induced by asymptotic constraints on the discrete solution (see [47, 48, 59, 60]). Specifically, the MITC3 formulation is applied within each triangular layer of the prismatic element [60–62]. In this approach, the in-layer strain components

$$\widetilde{E}_{13}, \quad \widetilde{E}_{23}, \quad \widetilde{E}_{q3} \stackrel{\mathrm{def}}{=} \widetilde{E}_{23} - \widetilde{E}_{13},$$

are evaluated at the quadrature points by reinterpolation from the associated tying points (denoted by the tilde$\widetilde{\ }$), while the in-plane strain components are left unmodified. This treatment is standard in 3D-shell discretizations and is necessary to obtain a mechanically consistent and thickness-robust response.

The contractile unknowns e_{c}^{n+1}, ϱ^{n+1} and γ^{n+1} in (20) are discretized in space using a collocation scheme at each quadrature point $\boldsymbol{q}_l$, $l = 1, \ldots, N_{\mathrm{q},h}$, where $N_{\mathrm{q},h} \stackrel{\mathrm{def}}{=} |\mathcal{T}_h| n_{\mathrm{q}}$ and n_{q} denotes the number of quadrature points in each element K of the mesh $\mathcal{T}_h$. This leads to $N_{\mathrm{q},h}$ degrees of freedom for each active variable, collected in the arrays:

$$\boldsymbol{e}_{\mathrm{c},h}^{n+1} \stackrel{\mathrm{def}}{=} \left\{ e_{\mathrm{c},l}^{n+1} \right\}_{l=1}^{N_{\mathrm{q},h}}, \quad \boldsymbol{\varrho}_h^{n+1} \stackrel{\mathrm{def}}{=} \left\{ \varrho_l^{n+1} \right\}_{l=1}^{N_{\mathrm{q},h}}, \quad \boldsymbol{\gamma}_h^{n+1} = \left\{ \gamma_l^{n+1} \right\}_{l=1}^{N_{\mathrm{q},h}}.$$

The proposed fully discrete approximation of the electromechanical problem (19) is summarized in Algorithm 1. The subscript l in the quantities $\boldsymbol{f}_l, \boldsymbol{E}_l^{n+\frac{1}{2}}, \widetilde{\boldsymbol{\Sigma}}_{\mathrm{p},l}^{n+\frac{1}{2}}, \widetilde{\boldsymbol{\Sigma}}_l^{n+\frac{1}{2}}, \boldsymbol{\Sigma}_a^{n+\frac{1}{2}}$ indicates their evaluation at the quadrature points $\boldsymbol{q}_l$, $l = 1, \ldots, N_{\mathrm{q},h}$. It is also noted that the passive stress $\widetilde{\boldsymbol{\Sigma}}_{\mathrm{p},l}^{n+\frac{1}{2}}$ depends on the reinterpolated Green-Lagrange strain tensor $\widetilde{\boldsymbol{\Sigma}}_l^{n+\frac{1}{2}}$. Furthermore, the discrete active variables $\boldsymbol{e}_{\mathrm{c},h}^{n+1}$, $\boldsymbol{\varrho}_h^{n+1}$ and $\boldsymbol{\gamma}_h^{n+1}$ can be eliminated at the element level through a Schur complement procedure (see [63]).

Algorithm 1 Fully discrete approximation of the 3D-shell electromechanical model (19).

For $n \geq 0$:

1. Find $(\boldsymbol{y}_h^{n+1}, \dot{\boldsymbol{y}}_h^{n+1}, \boldsymbol{e}_{\mathrm{c},h}^{n+1}, \boldsymbol{\varrho}_h^{n+1}, \boldsymbol{\gamma}_h^{n+1}, p_{\mathrm{at}}^{n+1}) \in \boldsymbol{V}_h^{\mathrm{sh}} \times \boldsymbol{V}_h^{\mathrm{sh}} \times \mathbb{R}^{N_{\mathrm{q},h}} \times \mathbb{R}^{N_{\mathrm{q},h}} \times (\mathbb{R}^+)^{N_{\mathrm{q},h}} \times \mathbb{R}$ with $\dot{\boldsymbol{y}}_h^{n+\frac{1}{2}} = \partial_\tau \boldsymbol{y}_h^{n+1}$ and such that

$$
\begin{cases}
\rho_{\mathrm{s}} \displaystyle\int_\Omega \partial_\tau \boldsymbol{u}_h^{n+1} \cdot \boldsymbol{v}_h + \int_\Omega \widetilde{\boldsymbol{\Sigma}}_{\mathrm{l}}^{n+\frac{1}{2}} : D_{\boldsymbol{y}} \widetilde{\boldsymbol{E}}^{n+\frac{1}{2}} \cdot \boldsymbol{v}_h + \int_\Omega \boldsymbol{\Sigma}_{\mathrm{a}}^{n+\frac{1}{2}} : D_{\boldsymbol{y}} \boldsymbol{E}^{n+\frac{1}{2}} \cdot \boldsymbol{v}_h \\
\quad + \displaystyle\int_{\Gamma_{\mathrm{mv}}} \left(a \boldsymbol{y}_h^{n+\frac{1}{2}} + b \dot{\boldsymbol{y}}_h^{n+\frac{1}{2}} \right) \cdot \boldsymbol{v}_h = - \int_{\Gamma_{\mathrm{en}}} J^{n+\frac{1}{2}} p_{\mathrm{at}}^{n+\frac{1}{2}} (\boldsymbol{F}^{n+\frac{1}{2}})^{-\top} \boldsymbol{n} \cdot \boldsymbol{v}_h, \\
\widetilde{\boldsymbol{\Sigma}}_l^{n+\frac{1}{2}} = \widetilde{\boldsymbol{\Sigma}}_{\mathrm{p},l}^{n+\frac{1}{2}} + \boldsymbol{\Sigma}_{\mathrm{a},l}^{n+\frac{1}{2}}, \quad \boldsymbol{\Sigma}_{\mathrm{a},l}^{n+\frac{1}{2}} = \dfrac{E_{\mathrm{s}} \left(\boldsymbol{f}_l^\top \boldsymbol{E}_l^{n+\frac{1}{2}} \boldsymbol{f}_l - e_{\mathrm{c},l}^{n+\frac{1}{2}} \right)}{\left(1 + 2 e_{\mathrm{c},l}^{n+\frac{1}{2}} \right)^2} \boldsymbol{f}_l \otimes \boldsymbol{f}_l, \\
\gamma_l^{n+1} \varrho_l^{n+1} + \mu_{\mathrm{c}} \partial_\tau e_{\mathrm{c},l}^{n+1} = E_{\mathrm{s}} \dfrac{\left(\boldsymbol{f}_l^\top \boldsymbol{E}_l^{n+\frac{1}{2}} \boldsymbol{f}_l - e_{\mathrm{c},l}^{n+\frac{1}{2}} \right) \left(1 + 2 \boldsymbol{f}_l^\top \boldsymbol{E}_l^{n+\frac{1}{2}} \boldsymbol{f}_l \right)}{\left(1 + 2 e_{\mathrm{c},l}^{n+\frac{1}{2}} \right)^3}, \\
\partial_\tau (\gamma_l^{n+1})^2 = - \left(\left| u_{\mathrm{e},l}^{n+1} \right| + \alpha_{\mathrm{d}} \left| \partial_\tau e_{\mathrm{c},l}^{n+1} \right| \right) (\gamma_l^{n+1})^2 + n_0(e_{\mathrm{c}}^n) k_0 \left| u_{\mathrm{e},l}^{n+1} \right|_+, \\
\partial_\tau \varrho_l^{n+1} = \gamma_l^{n+1} \partial_\tau e_{\mathrm{c},l}^{n+1} + \dfrac{n_0(e_{\mathrm{c}}^n) \sigma_0 \left| u_{\mathrm{e},l}^{n+1} \right|_+}{\gamma_l^{n+1}} \left(1 - \dfrac{k_0}{2 \sigma_0 \gamma_l^{n+1}} \varrho_l^{n+1} \right) \\
\quad - \dfrac{1}{2} \left(\left| u_{\mathrm{e},l}^{n+\frac{1}{2}} \right| + \left| \partial_\tau e_{\mathrm{c},l}^{n+1} \right| \right) \varrho_l^{n+1} = 0, \\
\displaystyle\int_{\Gamma_{\mathrm{en}} \cup \Gamma_{\mathrm{mc}}} J^{n+\frac{1}{2}} \dot{\boldsymbol{y}}_h^{n+\frac{1}{2}} \cdot \left(\boldsymbol{F}^{n+\frac{1}{2}} \right)^{-\top} \boldsymbol{n} = Q_{\mathrm{la}} \left(p_{\mathrm{vs}}(t_{n+\frac{1}{2}}), p_{\mathrm{lv}}^{n-\frac{1}{2}}, p_{\mathrm{at,l}}^{n+\frac{1}{2}} \right),
\end{cases}
\tag{25}
$$

   for all $\boldsymbol{v}_h \in \boldsymbol{V}_h^{\mathrm{sh}}$ and $l = 1, \ldots, N_{\mathrm{q},h}$.
2. Find $(y^{\mathrm{lv},n+1}, \dot{y}^{\mathrm{lv},n+1}, e_{\mathrm{c}}^{\mathrm{lv},n+1}, k_{\mathrm{c}}^{\mathrm{lv},n+1}, \tau_{\mathrm{c}}^{\mathrm{lv},n+1}, p_{\mathrm{lv}}^{n+1}) \in \mathbb{R}^6$ with $\dot{y}^{\mathrm{lv},n+\frac{1}{2}} = \partial_\tau y^{\mathrm{lv},n+1}$, such that (22) holds.

3 Results

This section presents the numerical results of the electromechanical simulations of the left atrium in physiological (Section 3.1) and pathological (Section 3.2) conditions. A series of numerical experiments has been carried out with the purpose of assessing the physiological relevance and computational benefits of the 3D-shell electromechanical model (19). To this purpose, the results obtained with the numerical method reported in Algorithm 1 are compared with those obtained with a standard $\mathbb{P}_1$ finite element approximation of the full 3D formulation (11). To ensure a rigorous comparison, constitutive electromechanical parameters and boundary conditions remain identical across all the 3D-shell and full 3D simulations.

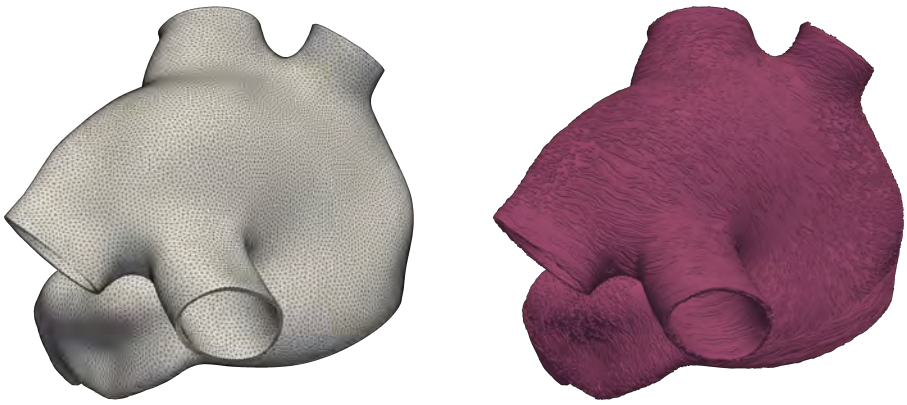

(a) Left-atrium mesh of Ω. (b) Fiber architecture.

Fig. 5: Geometry and fiber architecture of the left-atrium.

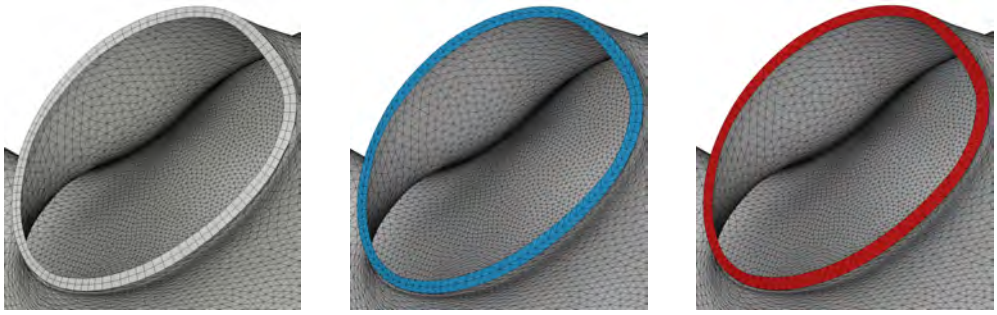

Fig. 6: The three types of spatial grids used in the numerical experiments. Left: $\mathbb{P}_1 \otimes \mathbb{P}_2$ (nine-nodes) prismatic elements (quadrilateral elements on the later faces). Middle: linear tetrahedral mesh with two layer of elements. Right: linear tetrahedral mesh with one layer of elements.

	3D-shell	**3D (2-layer)**	**3D (1-layer)**
Number of nodes	59,574	59,574	39,716
Number of cells	39,131	234,786	117,393
Hours per cycle	2.25	3.7	2.11
Total compute hours	15.8	26.06	14.77
Memory per MPI process	300 MB	600 MB	350 MB
Avg. Newton iterations	4	6	5

Table 1: Mesh details, execution times, memory and entity count per test case.

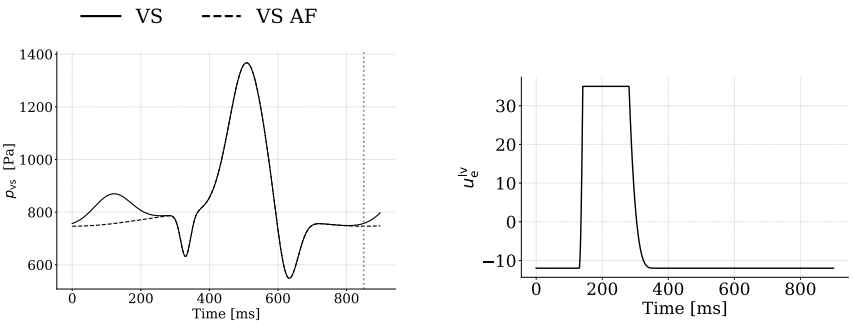

(a) Pulmonary veins pressure p_{vs}.

(b) LV activation profile $u_{\mathrm{e}}^{\mathrm{lv}}$.

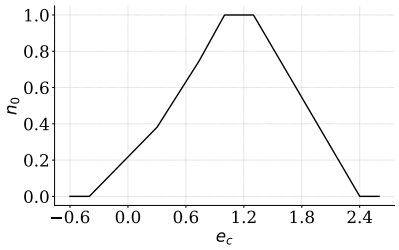

(c) Starling reduction factor $n_0(e_{\mathrm{c}})$.

Fig. 7: Imposed data curves for the pulmonary veins pressure, the electrical activation for the left-ventricle model, and the profile for n_0.

The considered left atrial geometry was extracted from the Zygote heart model[1], from which the internal and external surfaces where smoothed and refined (see Fig. 5a). Specifically, localized smoothing was applied to the endocardial and epicardial surfaces of the left atrial appendage (LAA) and the junction between the LAA and the pulmonary veins, to prevent the generation of sharp elements. These geometric treatments were performed using the 3-Matic[2] software. The final computational mesh consists of a single layer of triangular prismatic elements, generated by extruding the epicardial surface along its local inward normal direction. The spatial heterogeneity of the atrial wall was captured by defining the local thickness as the point-wise Euclidean distance between the reference epicardial and endocardial surfaces. This distance is computed using the closest point projection algorithm (see, e.g., [64]) and is explicitly imposed during the mesh generation process to ensure a geometrically accurate reconstruction. Since anatomical geometries such as the Zygote model typically correspond to a loaded state, a pre-stressing procedure is employed to recover an approximate stress-free reference configuration of the left atrium (see, e.g., [65, 66]), ensuring that the application of physiological loads reproduces the target geometry with a consistent

[1] https://www.zygote.com
[2] https://www.materialise.com

Parameter	Description	Value	Unit
R_0	Reference LV radius	2.6×10^{-2}	m
d_0	Reference wall thickness	1.7×10^{-2}	m
ρ	Myocardial density	1000	kg/m^3
η	Viscous coefficient in Σ_{sph}	70	–
C_0	Passive stiffness parameter (isotropic)	1.9×10^3	Pa
C_1	Passive exponent parameter (isotropic)	1.1×10^{-1}	–
C_2	Passive stiffness parameter (anisotropic)	1.9×10^3	Pa
C_3	Passive exponent parameter (anisotropic)	1.1×10^{-1}	–
E_{s}^{lv}	Active stiffness modulus	3×10^5	Pa
k_{ar}	Aortic valve conductance	1.3×10^{-5}	m^3/Pa·s
R_{p}	Proximal resistance	8×10^6	Pa·s/m^3
R_{d}	Distal resistance	1×10^8	Pa·s/m^3
C_{p}	Proximal compliance	5×10^{-9}	m^3/Pa
C_{d}	Distal compliance	1×10^{-8}	m^3/Pa
t_{d}	Activation delay	130	ms
t_{dep}	Depolarization duration	11	ms
t_{plat}	Plateau duration	140	ms
t_{rep}	Repolarization duration	80	ms
$u_{\max}$	Maximum activation potential	35	mV
$u_{\min}$	Minimum activation potential	-12	mV
c_{w}	Conduction wave velocity	0.6	m/s

Table 2: Parameters of the lumped-parameter left-ventricle model.

stress state, resulting in the final mesh reported in Fig. 5a. Finally, the planar surface closure Γ_{mc} is triangulated without node insertion, using only the inner edges of Γ_{mv}.

The fiber architecture (see Fig. 5b) is subsequently generated on the computational mesh by using an adaptation of the Laplace-Dirichlet Rule-Based (LDRB) framework proposed in [16]. Unlike the standard volumetric approach, the algorithm is applied separately to the epicardial and endocardial surfaces to capture the significant transmural variations in fiber orientation [67, 68], with the wall-transverse distribution interpolated according to [69] (see Appendix B).

In this work, three spatial discretizations of the atrial wall are evaluated and compared (see Fig. 6):

- the prismatic $\mathbb{P}_1 \otimes \mathbb{P}_2$ approximation provided by the 3D-shell formulation of Algorithm 1;
- a standard $\mathbb{P}_1$ approximation of the full 3D formulation (11) using single-layer tetrahedral mesh;
- a standard $\mathbb{P}_1$ approximation of the full 3D formulation (11) using a two-layer tetrahedral mesh.

To guaranty a consistent comparison between the shell and solid models, both tetrahedral meshes are derived from the same base 9-node prismatic mesh. The two-layer configuration is generated by subdividing each prism through its thickness (see, e.g.,

Parameter	Description	Value	Unit
a_{p}	Passive matrix stiffness parameter	$6 \cdot 10^3$	Pa
b_{p}	Passive matrix exponential coefficient	5.5	–
a_{f}	Fiber stiffness parameter	$12 \cdot 10^3$	Pa
b_{f}	Fiber exponential coefficient	11.75	–
κ	Bulk modulus penalization parameter	$4 \cdot 10^5$	Pa
ν	Passive viscosity coefficient	1000	$\mathrm{N} \cdot \mathrm{s} \cdot \mathrm{m}^{-2}$
E_{s}	Elastic stiffness of sarcomere element	$5 \cdot 10^4$	Pa
k_0	Maximum active stiffness	$1 \cdot 10^5$	Pa
σ_0	Intrinsic active stress (contractility constant)	$2 \cdot 10^6$	Pa
μ_{c}	Active viscous coefficient (contractile branch)	100	$\mathrm{N} \cdot \mathrm{s} \cdot \mathrm{m}^{-1}$
k_{mv}	Conductance of mitral valve	$8 \cdot 10^{-7}$	$\mathrm{m}^3 \cdot \mathrm{s}^{-1} \cdot \mathrm{Pa}^{-1}$
k_{vs}	Conductance of pulmonary veins	$5 \cdot 10^{-7}$	$\mathrm{m}^3 \cdot \mathrm{s}^{-1} \cdot \mathrm{Pa}^{-1}$
α_{d}	Cross-bridge destruction coefficient	3.0	–
α	Activation scaling for V_{m}	0	–
β	Activation offset for V_{m}	1	–
a	Viscoelastic displacement parameter	$1 \cdot 10^5$	–
b	Viscoelastic velocity parameter	$1 \cdot 10^7$	–

Table 3: Constitutive parameters of the 3D-shell electromechanical model.

[70]), while the single-layer mesh is constructed by first reducing the prism to a 6-node wedge prior to subdivision. This strategy ensures that all discretizations share an identical mid-surface and boundary triangulation, providing a coherent framework for analyzing their mechanical responses. The resulting element and node counts are detailed in Table 1.

All simulations employ the same passive and active material parameters and the same mechanical boundary conditions and have been run at a time resolution of $\tau = 10^{-3}$ s. The constitutive parameters of the Demiray-Gasser law, the viscous regularization, and the active contraction model are identical in all test cases (see Table 3). The imposed analytic data curves for the pulmonary veins pressure of the electromechanical model (14), the imposed electrical activation of the left ventricle model (16), and the scaling factor profile n_0 relative to the fiber elongation are reported in Fig. 7.

Each simulation is run over seven cardiac cycles to eliminate initial transients and to reach a periodic solution. The electromechanical coupling strategy, the time-integration scheme, as well as the nonlinear solvers and tolerances are kept fixed throughout, thereby providing a controlled setting for analyzing the influence of the spatial discretization on the predicted deformation and computational cost.

All simulations were performed using the open-source finite element library `FELiScE`[3] on a 2023 Mac Studio equipped with 128 GB of RAM and an Apple M2 Ultra

[3] https://gitlab.inria.fr/felisce/felisce

processor, using 12 cores. The resulting execution times, memory usage, discretization sizes and average number of Newton iterations per timestep for each mesh are reported in Table 1.

3.1 Normal condition

In this section, we present the numerical results of the electromechanical simulations of the left atrium under physiological conditions.

Electrical propagation

The transmembrane potential V_{m} involved in the electrical input (2) is obtained by using the bidomain model (see Appendix A for furhter details). The atrial tissue is assumed to be initially repolarized, with $V_{\mathrm{m}}(\cdot, 0) = -81.2$ mV in Ω. Electrical activation is initiated at Bachmann's bundle. Fig. 8 reports some snapshots of the

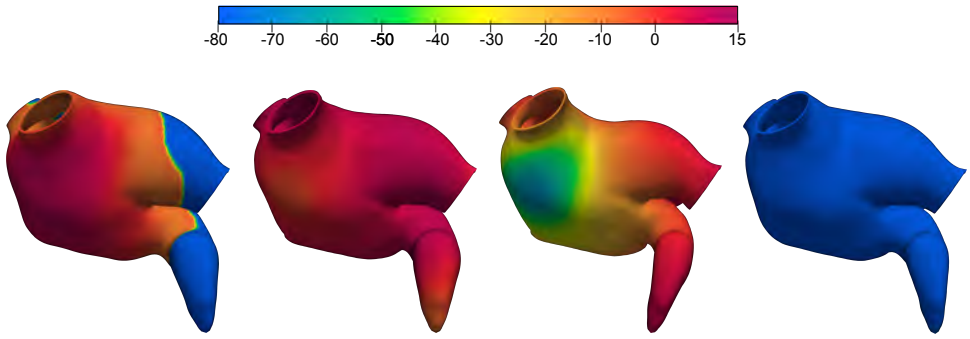

(a) $t = 50$ ms. (b) $t = 100$ ms. (c) $t = 150$ ms. (d) $t = 250$ ms.

Fig. 8: Left atrium transmembrane potential V_{m} used as electrical activation in all physiological simulations.

transmembrane potential at different time instants. The activation wave originates in the anterior wall near Bachmann's bundle and propagates throughout the chamber. At $t = 50$ ms, the wavefront has advanced significantly across the anterior region, with accelerated propagation along Bachmann's bundle. By this time, the wave has also reached the atrial roof and starts its progression towards the middle section of the posterior part of the left atrium. At $t = 100$ ms, depolarization covers nearly the entire domain, with only the apex of the left atrial appendage remaining inactivated. Finally, repolarization of the atrial wall starts at around $t = 150$ ms near the Bachmann's bundle, and the tissue is fully repolarized by $t = 250$ ms. These activation patterns are in good agreement with physiological observations reported in the literature (see, e.g., [16, 71, 72]).

3D-shell model

The temporal evolution of left atrial pressure, volume and pressure-volume loop obtained with the 3D-shell model (Algorithm 1) are reported in Fig. 9. These reulsts show reasonable agreement with experimental and numerical data reported in the literature (see, e.g., [46, 73, 74]). In particular, they accurately capture the characteristic three-phase function of the atrium. Initially, the booster pump phase is observed,

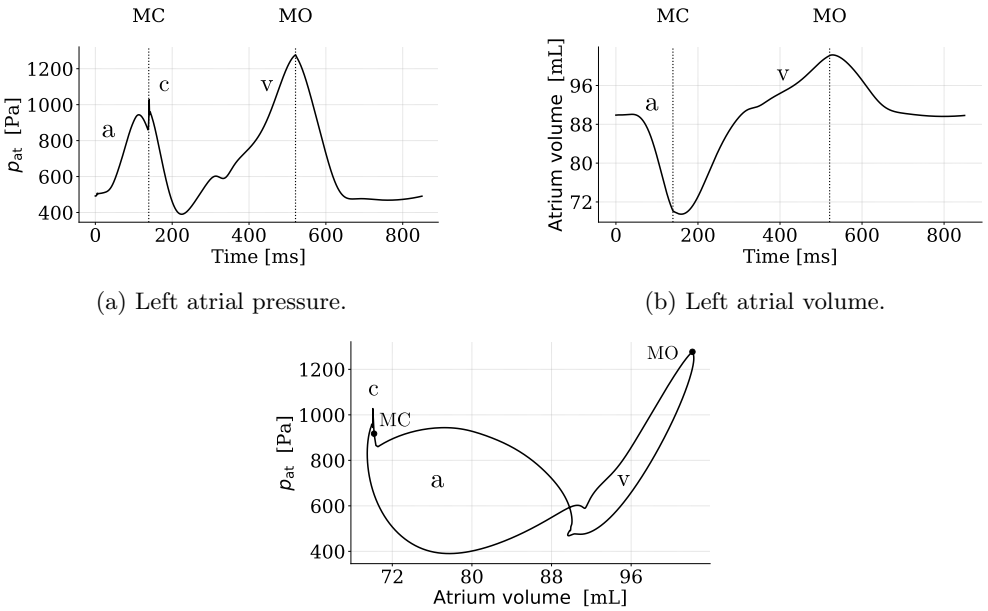

(a) Left atrial pressure.

(b) Left atrial volume.

(c) Pressure–volume loop.

Fig. 9: Left atrial pressure, volume and pressure-volume loop obtained the 3D-shell model (Algorithm 1) under healthy conditions.

characterized by a reduction in volume driven by active atrial contraction (a-wave). This is accompanied by a sustained increase in atrial pressure. As the atrium starts to repolarize, the pressure begins to decrease. Subsequently, the closure of the mitral valve marks the beginning of the reservoir phase. This phase is characterized by a temporary pressure spike (c-wave), followed by a pressure decrease as the atrium continues to relax. Then, both volume and pressure begin to rise due to inflow from the pulmonary veins (v-wave). As the atrium approaches its maximum capacity, the rate of filling slows down while the pressure increases more rapidly. Finally, the mitral valve reopens to start the conduit phase. This results in a sharp drop in both volume and pressure (y-wave). As the left ventricle fills, the emptying rate slows, eventually reaching a point where both variables remain nearly constant. The pressure-volume loop

(Fig. 9c) exhibits the characteristic eight-shape of the left atrium, with both the a-loop and v-loop displaying shapes consistent with the literature, though with a bigger a-loop than v-loop which is usually expected to be the opposite.

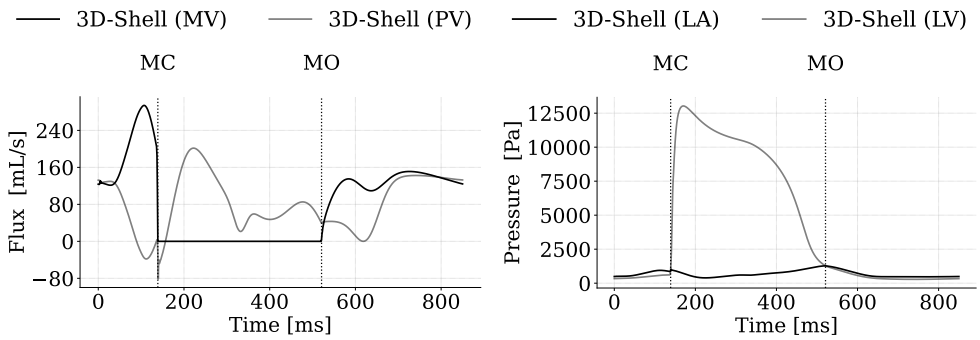

(a) Fluxes through pulmonary veins (PV) and mitral valve (MV).

(b) Pressure curves for left atrium (LA) and left ventricle (LV).

Fig. 10: Fluxes and pressures obtained with the 3D-shell model (Algorithm 1) under healthy conditions.

Fig. 10a shows the flux evolution across the pulmonary veins and the mitral valve. During atrial contraction (a-wave), the flow through the pulmonary veins is reduced. This is followed by the systolic forward flow (c-wave), characterized by a continuous decrease in pulmonary inflow immediately after the mitral valve closes. This flux reaches a minimum at the late systolic phase of the left ventricle (see Fig. 10b), marking the transition to diastolic forward flow (v-wave). This phase features a gradual increase in flow as the left atrial pressure converges with the pulmonary venous pressure, which produces a sustained decrease in the flux eventually reaching a plateau phase. Following this stabilization, the opening of the mitral valve (y-wave) marks a sudden decrease in the flux across the pulmonary veins followed by a sustained increase as the atrial pressure drops. Finally, the flux in the pulmonary veins reaches a plateau phase just before the next contraction begins. On the other hand, flow through the mitral valve becomes maximal during atrial contraction. This flow decreases as the left atrium begins to relax, eventually reaching zero when the mitral valve closes (at the beginning of the c-wave). The closure of the valve, induced by the pressure increase within the left ventricle, marks the start of the left atrial filling phase, characterized by zero flux through the mitral valve under physiological conditions. Finally, the mitral valve opens when the atrial pressure exceeds the ventricular pressure. This gradient drives a sustained increase in flow across the valve, followed by a plateau phase as the atrial and ventricular pressures converge (see Fig. 10a). The pressure evolution within the left ventricle (see Fig. 10b) exhibits physiological behavior, where the opening and closing of the mitral valve are dictated by the pressure gradient between the atrium and the ventricle, showing the hemodynamic coupling between these two chambers.

The left atrial pressure evolution remains within physiological ranges, reaching a minimum of 390.26 Pa at the end of the relaxation phase and a maximum of 1277.07 Pa at the end of the filling phase (see, e.g., [67, 73, 75, 76]). However, the volume variation is slightly lower than values reported in the literature (see, e.g., [77]). The atrial ejection fraction (EF) is defined as

$$\mathrm{EF} \stackrel{\mathrm{def}}{=} \frac{\mathrm{V_{max}} - \mathrm{V_{min}}}{\mathrm{V_{max}}},$$

where $\mathrm{V_{max}}$ and $\mathrm{V_{min}}$ represent the maximum and minimum internal volumes of the left atrium, respectively. The computed ejection fraction is $\mathrm{EF} = 32,08\%$, with minimum and maximum volumes of $\mathrm{V_{min}} = 69.48$ mL and $\mathrm{V_{max}} = 102.29$ mL. This value falls slightly below the physiological range of [45%–60%] typically reported in the experimental literature (see, e.g., [78–80]).

Another relevant parameter is the stroke volume (SV), which quantifies the total volume of blood ejected by the left atrium during a single cardiac cycle, and is formally defined as $\mathrm{SV} \stackrel{\mathrm{def}}{=} \mathrm{V_{max}} - \mathrm{V_{min}}$. Furthermore, this metric can be decomposed into passive and active contributions, corresponding to the atrial conduit (early diastolic) and contractile (booster pump) phases, respectively. The stroke volume for the atrial conduit phase is $\mathrm{SV_p} = 12.48$ mL, while the contribution from the atrial pump phase is $\mathrm{SV_a} = 20.41$ mL, yielding a total stroke volume of $\mathrm{SV} = 32.89$ mL (see, e.g., [80]).

Finally, a key parameter to quantify the mechanical energy generated by the left atrium during the conduit and booster pump phases is the stroke work (SW). This metric corresponds to the area enclosed by the pressure-volume loop and is calculated as $\mathrm{SW} \stackrel{\mathrm{def}}{=} \oint p_{\mathrm{at}}(\mathrm{V})\mathrm{dV}$. Similar to the stroke volume, the total stroke work is partitioned into the specific work performed during the active atrial pump phase and the passive conduit phase. The computed values are $\mathrm{SW_p} = 16.06$ mmHg mL and $\mathrm{SW_a} = 60.85$ mmHg mL, respectively, producing a total stroke work of $\mathrm{SW} = 76.91$ mmHg mL.

3D-shell vs. full 3D formulation

The numerical results show that the spatial discretization has a significant impact on the predicted electromechanical response of the left atrium under physiological conditions. In particular, the single-layer tetrahedral discretization fails to reproduce a physically plausible evolution of the atrial volume, pressure, and flow (see Fig. 11).

This phenomenon is evidenced throughout the left atrial cardiac cycle, which is characterized by active contraction followed by relaxation and passive filling. While this sequence is accurately captured by the 3D-shell formulation, the single-layer tetrahedral mesh exhibits an artificially stiff response that delays atrial filling This results in a non-physiological phase characterized by negligible volume changes—essentially a spurious plateau—which fails to represent the compliant nature of the atrial wall during diastole. Consequently, this lack of compliance prevents the model from accurately mimicking the pressure-volume relationship required for realistic hemodynamic simulations. On the other hand, introducing a second layer of tetrahedral elements substantially improves the mechanical response. The two-layer tetrahedral mesh recovers realistic pressure, volume, and flow evolutions that are in close agreement with the

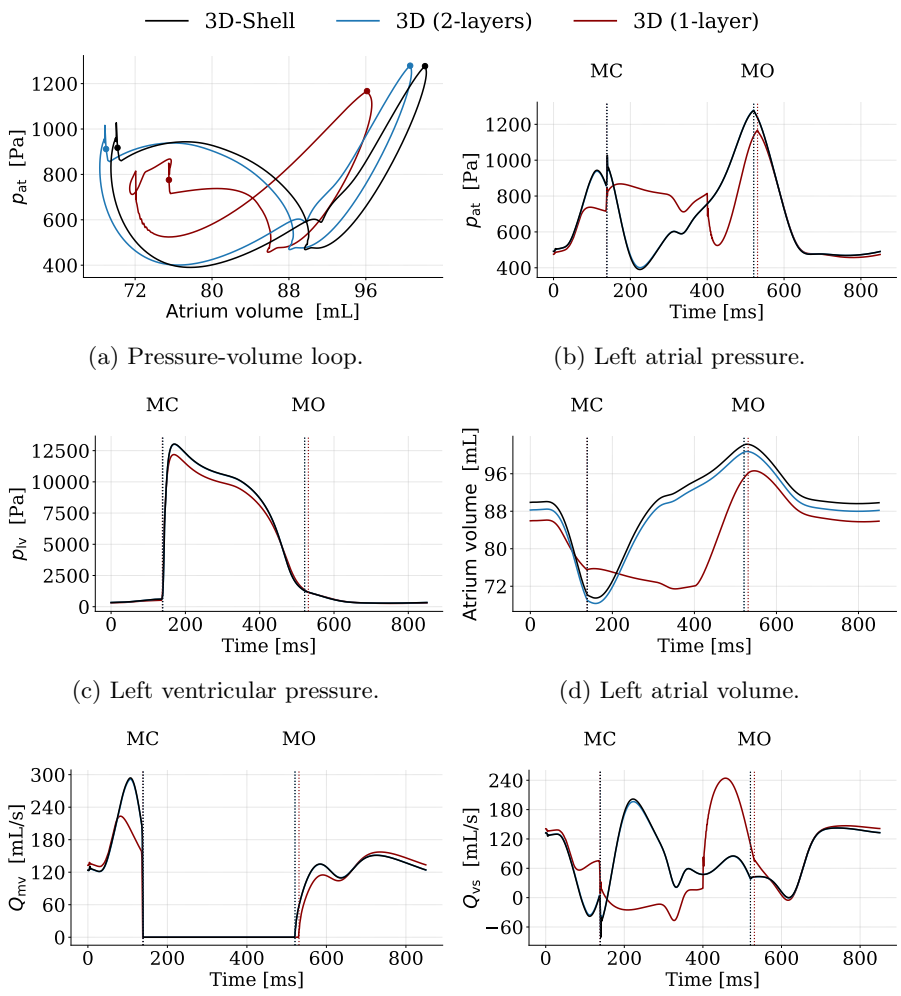

(a) Pressure-volume loop.

(b) Left atrial pressure.

(c) Left ventricular pressure.

(d) Left atrial volume.

(e) Mitral valve flux.

(f) Pulmonary veins flux.

Fig. 11: Comparison of pressures, volumes, and fluxes for the three discretizations (3D-shell, 3D two-layer tetrahedral, 3D one-layer tetrahedral) under healthy conditions.

shell results. However, this improvement comes at the cost of increasing the number of elements from 39,131 prismatic elements to 234,786 tetrahedra, resulting in a 1.6-fold increase in execution time (see Table 1). Similar observations, can be inferred from Figs. 12 and 13, which reports some snapshots of the displacement in the deformed configuration obtained with the 3D-shell and the full 3D formulations.

Finally, Table 4 presents several relevant physiological biomarkers comparing the 3D-shell model with the one- and two-layer 3D tetrahedral models. As observed, the

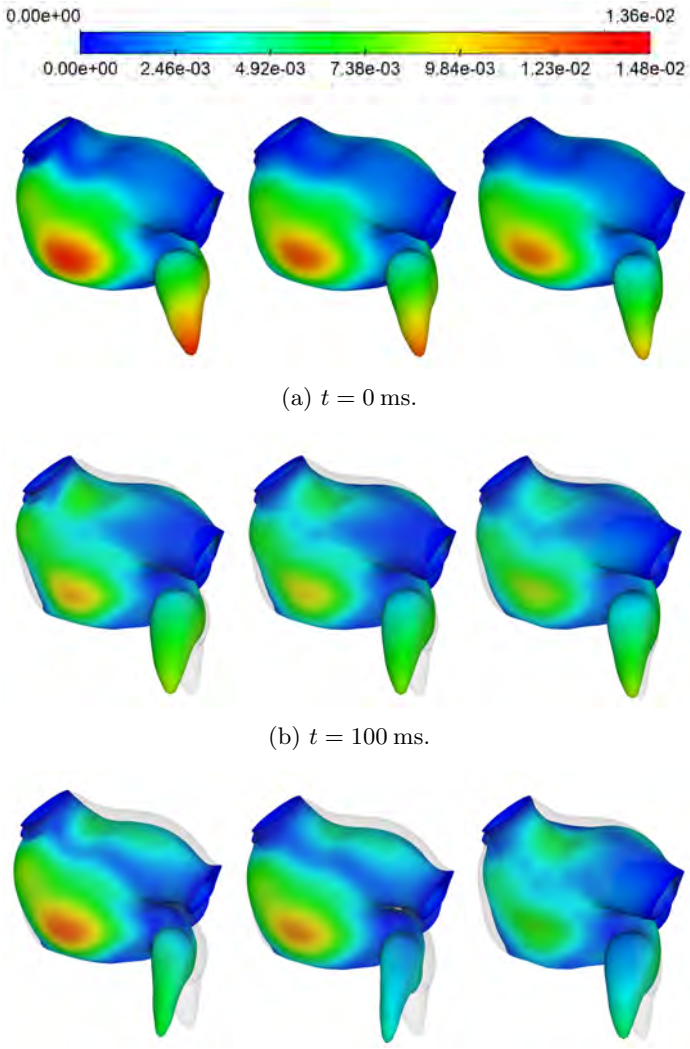

(a) $t = 0$ ms.

(b) $t = 100$ ms.

(c) $t = 200$ ms.

Fig. 12: Snapshots of the atrial displacement in deformed configuration. Left: 3D-shell model; Middle: 3D (2-layers); Right: 3D (1-layer).

3D-shell and the two-layer tetrahedral formulations yield lower minimum and higher maximum volumes of similar magnitude, contrasting with the restricted range of the single-layer case. This trend is also preserved in the pressure evolution, where the 3D-shell and two-layer models achieve lower minimum and higher maximum pressures. Notably, the 3D-shell model retrieves the highest stroke volume and ejection fraction, exceeding the single-layer 3D model by around 30.2%. Finally, the comparison among the stroke works reveals that the single-layer model provides a notably inferior stroke

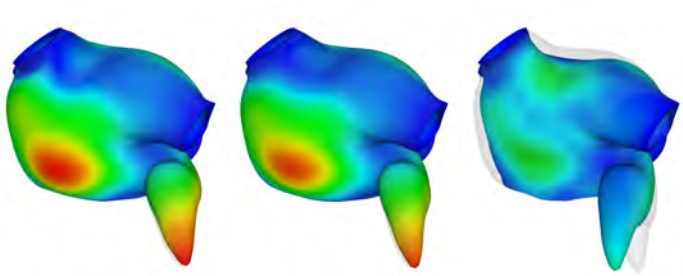

(a) $t = 300$ ms.

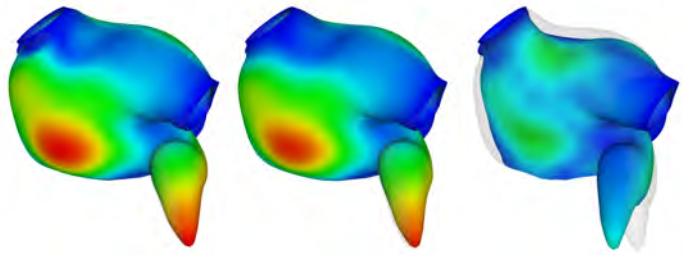

(b) $t = 400$ ms.

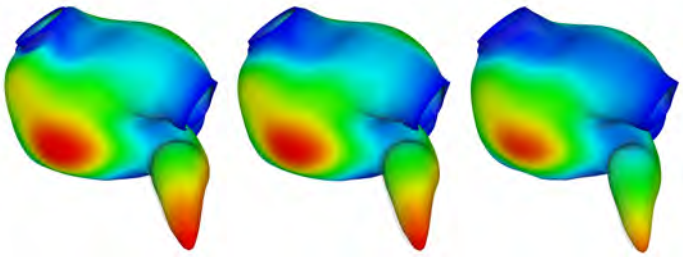

(c) $t = 500$ ms.

Fig. 13: Snapshots of the atrial displacement in deformed configuration. Left: 3D-shell model; Middle: 3D (2-layers); Right: 3D (1-layer).

work during the active pumping phase, representing only approximately 20% of the work performed by the 3D-shell and 3D two-layer models.

3.2 Pathological condition

This section presents the numerical results of left atrial electromechanics under the pathological condition of atrial fibrillation, a cardiac pathology that disrupts normal electrical propagation, leading to irregular and chaotic activity. Specifically, this condition alters the standard activation wavefronts, generating rotors or spiral waves throughout the left atrium (see, e.g., [81]).

Variable	3D-Shell	3D (2-layer)	3D (1-layer)	Unit
V_{min}	69.48	68.32	71.53	mL
V_{max}	102.30	100.75	96.62	mL
p_{min}	390.26	400.53	457.16	Pa
p_{max}	1277.07	1279.14	1167.03	Pa
SV_p	12.48	12.56	10.74	mL
SV_a	20.41	19.93	14.52	mL
SV	32.89	32.50	25.26	mL
EF	32.08	32.18	26.07	-
SW_p	16.06	16.23	24.67	mmHg mL
SW_a	60.85	57.97	14.22	mmHg mL

Table 4: Main biomarkers for different spatial approximations (healthy condition).

Electrical activation

The disruption of electrical propagation results in a weak and disorganized wavefront that, from a biomechanical perspective, is insufficient to trigger a significant mechanical contraction, leading to the absence of the atrial kick. Accordingly, this state is modeled using (19) as for the physiological case, but with the left atrial active tension set to zero, viz., $\boldsymbol{\Sigma}_a = \mathbf{0}$. This approach is consistent with numerous electromechanical studies on atrial fibrillation (see, e.g., [39, 40, 82–85]). Furthermore, the impact of atrial fibrillation extends to the pulmonary veins. Accordingly, the pulmonary venous pressure profile imposed in these pathological example lacks of a- and c-waves (see dotted line in Fig. 7a).

3D-shell model

Fig. 14 compares the evolution of pressure, volume, the pressure-volume loop, the left ventricular pressure, and the transmitral and veins fluxes obtained with the 3D-shell model (Algorithm 1) for the healthy and AF conditions. As observed, during atrial fibrillation (AF), the atrium loses its ability to contract effectively, leading to the absence of the atrial kick and a subsequent alteration of all hemodynamic quantities. Specifically, the pressure evolution in the AF case lacks the characteristic pressure increase associated with the atrial kick (a-wave).

Furthermore, following mitral valve closure, the pressure in the AF model exhibits a continuous rise, contrasting with the physiological case where a relaxation phase typically lowers the pressure before the reservoir phase begins. Conversely, upon mitral valve opening, the y-wave remains similar in both scenarios, indicating that AF primarily impacts the active contractile phase rather than passive filling. The evolution of the volume shows that during the atrial kick phase, the atrium under AF conditions fails to contracts, and thus does not reduce its volume. Consequently, immediately following mitral valve closure, the volume continues to increase during the v-wave, reaching a slightly larger maximum volume compared to the physiological case. When the mitral valve subsequently opens, the passive volume decrease (early filling) remains similar to the physiological baseline. These alterations are distinctly reflected in the

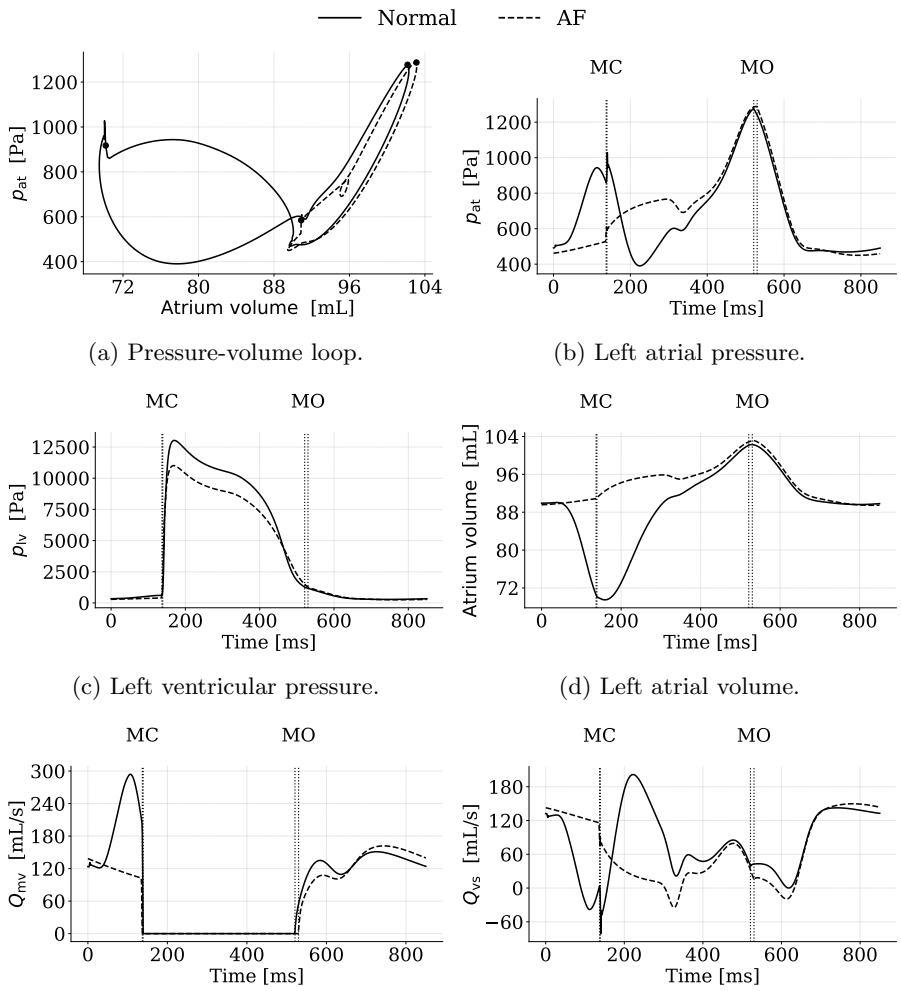

(a) Pressure-volume loop.

(b) Left atrial pressure.

(c) Left ventricular pressure.

(d) Left atrial volume.

(e) Mitral valve flux.

(f) Pulmonary veins flux.

Fig. 14: Comparison between healthy (continuous lines) and atrial-fibrillation (dashed lines) conditions obtained with the 3d-shell model (Algorithm 1).

pressure-volume loop, which notably lacks the active a-loop component during the pathological case.

Furthermore, the simulation of AF demonstrates a decrease in left ventricular preload, as indicated by the absence of the atrial kick. This reduction in filling subsequently lowers the maximum pressure developed within the left ventricle during the pathological cycle. Finally, the flux through the mitral valve shows that there is a decrease in the mitrral flux during the atrial kick for the case of AF, which is expected since the atrium is solely passively filled during this pathology. Then, upon the opening

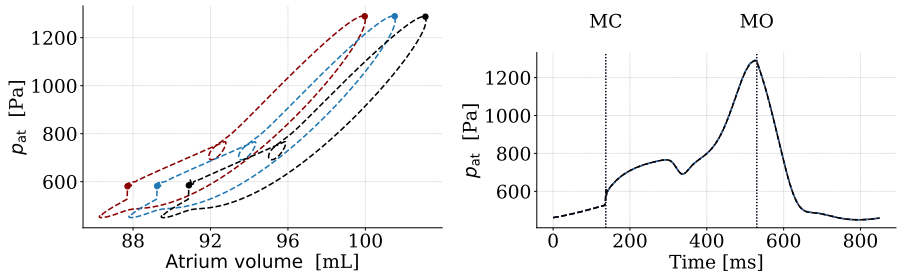

(a) Pressure-volume loop.

(b) Left atrial pressure.

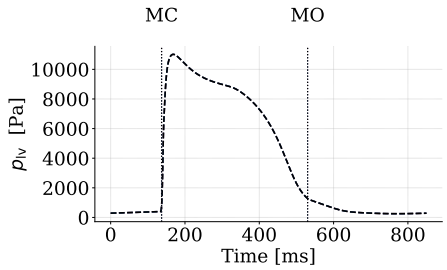

(c) Pressure curve for the left ventricle.

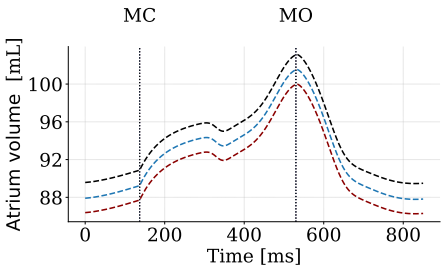

(d) Volume curve for the left atrium.

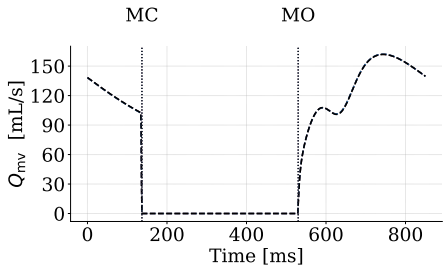

(e) Flux across the mitral valve.

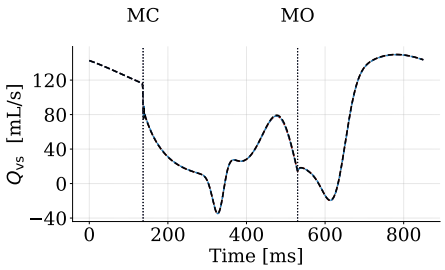

(f) Flux across the pulmonary veins.

Fig. 15: Comparison of pressures, volumes, and fluxes for the three discretizations (3D-shell, 3D two-layer tetrahedral, 3D one-layer tetrahedral) under atrial-fibrilation.

of the mitral valve, the transmitral flux is nearly identical in both cases. In contrast, the flux through the pulmonary veins remains nearly constant during the late diastolic phase in the AF model. This stability results from the absence of the atrial kick, which impulse significant pressure variations within the pulmonary veins or the left atrium during this interval. Subsequently, upon mitral valve closure, the venous flux suffers a sudden drop as the left atrial pressure rises and approaches to the pressure in the pulmonary veins. Finally, once the mitral valve opens, the flow profile resembles the physiological case, initially slightly decreasing due to the predominance of the high transmitral flux, before increasing again as the pressure in the left atrium decreases.

3D-shell model vs. full 3D

Under atrial fibrillation, the absence of coordinated atrial contraction leads to a mechanical response dominated by low-amplitude, pressure-driven deformations. In this regime, all discretizations yield nearly identical pressure, volume, and flow evolutions, as shown in Fig. 15, up to minor shifts attributable to compliance differences between discretizations.

4 Discussion

The results reported in Section 3 show that the proposed 3D–shell formulation reproduces the essential electromechanical behavior of the left atrium at a substantially lower computational cost than standard 3D solid formulations. This is supported by the pressure–volume dynamics, deformation patterns, and flow profiles shown in Figs. 9 and 11, together with the execution times and memory usage reported in Table 1. The proposed 3D-shell model of atrial electromechanics integrates physiological electrical activation sequences, uadratic through-thickness shell kinematics with MITC3 re-interpolation, transmural fiber architecture, atrium-specific active constitutive law, and the coupling with a dedicated 0D electromechanical model of the left ventricle.

As mentioned in Section 2.1.1, the thin-walled nature of the left atrium introduces a structural limitation in standard displacement-based 3D formulations such as $(11)_1$. When the wall thickness is small relative to the in-plane dimensions, low-order kinematic approximations lead to an artificially stiff response unless several elements are introduced across the thickness. This limitation is clearly observed in the single-layer tetrahedral discretization, which fails to reproduce a realistic evolution of atrial volume, pressure, and flow under physiological conditions (see Figs. 11 and 12). As shown in [48], this behavior is not a numerical locking artifact *per se*, but rather a modeling inconsistency induced by the fact that linear through-thickness kinematics are not asymptotically consistent with classical shell models as the thickness tends to zero. The artificial stiffening observed in the results of Section 3 therefore provides numerical evidence of this model inconsistency.

The 3D–shell formulation resolves this issue by adopting a quadratic behavior of the displacement field through the thickness. This kinematic assumption restores asymptotic consistency while retaining a fully 3D constitutive framework. In practice, this leads to a robust mechanical response, evidenced by larger displacement amplitudes, a realistic relaxation phase, and physiologically consistent pressure–volume loops (see Figs. 9 and 11), without requiring through-thickness mesh refinement.

Under physiological conditions, where active contraction induces large deformation gradients, the mechanical response is therefore critically dependent on the spatial discretization. Single-layer tetrahedral meshes systematically underestimate deformation and pressure amplitudes, leading to delayed relaxation, distorted pressure-volume dynamics, and altered flow patterns (Fig. 11). Introducing a second tetrahedral layer recovers pressure, volume, and flow evolutions comparable to those of the 3D–shell formulation, but at the cost of a nearly six-fold increase in element count and a 1.6-fold increase in execution time (Table 1). The 3D-shell formulation achieves comparable accuracy at a reduced computational cost.

In contrast, under atrial fibrillation, the absence of coordinated atrial contraction results in a mechanical response dominated by low-amplitude, pressure-driven deformations. In this regime, all discretizations yield nearly identical pressure, volume, and flow evolutions (Fig. 15), up to minor shifts attributable to compliance differences. This behavior follows directly from the kinematic regime involved: when deformation amplitudes remain small, the asymptotic inconsistency of low-order through-thickness kinematics identified in [48] is not activated. These results are in agreement with clinical observations and with previously reported numerical studies of AF (see, e.g., the previous work [51]).

Accurate estimation of left ventricular preload relies on a compliant mechanical response of the left atrium [86–89]. Inaccurate atrial pressure predictions therefore propagate directly to the ventricular response. The single-layer tetrahedral discretization systematically underestimates preload relative to both the two-layer and 3D–shell models (see Fig. 11c), resulting in reduced ventricular filling. Consistently, the hemodynamic analysis shows that the 3D–shell and two-layer discretizations produce nearly identical mitral and pulmonary venous flow profiles, whereas the single-layer mesh underestimates mitral inflow and delays the pulmonary venous v-wave peak, reflecting an artificial attenuation of atrial compliance.

While the proposed 3D-shell formulation incorporates the MITC3 technique to prevent shear locking, numerical evidence (not reported here) indicates that similar mechanical responses are obtained with and without the MITC3 reinterpolation. This suggests that shear locking is not a dominant numerical issue in the present application. Indeed, since the atrial tissue undergoes significant inflation and stretching, the deformation is likely membrane-dominated, such that shear locking is not a fundamental here. Nevertheless, owing to the complex and non-uniform kinematics of the left atrium under physiological and pathological conditions, the occurrence of other locking modes cannot be entirely excluded. A truly robust model of the left atrium would therefore benefit from advanced finite element formulations capable of accounting for all potential locking phenomena (see, e.g., [48, 49, 90]).

From a clinical perspective, 3D–shell modeling of the left atrium constitutes a meaningful step toward numerically reliable patient-specific simulations, as required by emerging digital-twin approaches (see, e.g., [91–93]). Applications such as atrial fibrillation analysis or catheter ablation planning require mechanically accurate predictions at a computational cost compatible with routine use, making spatial discretization a decisive modeling choice rather than a secondary numerical detail. The present results show that single-layer tetrahedral discretizations, although inexpensive, fail to deliver physiologically consistent atrial mechanics and systematically underestimate ventricular filling, stroke volume, and cardiac output. While two-layer tetrahedral meshes recover accuracy, their computational and memory costs limit their practical applicability [94, 95]. By contrast, the 3D–shell formulation provides a compliant and mechanically consistent atrial response without through-thickness refinement, offering a more favorable balance between accuracy and efficiency for clinically oriented electromechanical simulations.

5 Limitations

Despite the advantages of the proposed 3D-shell electromechanical model of the left atrium, several limitations of the present work warrant discussion. First, the model does not include a fully coupled 3D–0D closed-loop model of circulation. In the current formulation, venous inflow is prescribed through an imposed pressure profile (Fig. 7a), which lacks the dynamic feedback mechanisms inherent to a closed-loop system. Consequently, venous pressure does not adapt to changes in atrial or ventricular hemodynamics. A natural extension of this work would be the incorporation of a complete closed-loop circulation model, similar to the approach reported in [44]. Nevertheless, such an extension lies beyond the primary scope of this study, whose central objective is to investigate the benefits of the 3D-shell modeling of the left atrium. Second, mechanical contact with the pericardial sac is neglected. The pericardium provides a physical constraint that can significantly limit atrial motion, particularly during rapid filling phases or under pathological conditions such as constrictive pericarditis (see, e.g., [30, 36, 96]). Third, the left atrium and left ventricle exhibit strong mechanical interdependence. From this perspective, coupling the present atrial 3D-shell model with a 3D electromechanical model of the left ventricle would be desirable to improve both the predicted atrial and ventricular function. Such a multi-chamber framework would also enable the representation of longitudinal mitral annular motion, which plays a key role during atrial filling. A major strength of the proposed formulation lies in its suitability as a calibration platform for more advanced modeling frameworks, including fluid–structure interaction (FSI) models of the left atrium. The incorporation of 3D fluid dynamics is essential for a comprehensive description of both chamber hemodynamics and tissue mechanics. While several studies have investigated atrial hemodynamics and their influence on left ventricular flow patterns (see [97–99]), only a limited number have addressed the fully coupled FSI problem, owing to its substantial complexity and computational cost (see [52, 100–102]). In this context, the proposed 3D-shell electromechanical model represents a natural step toward a robust and computationally efficient FSI framework (see [103]).

6 Conclusion

This work introduces a 3D-shell electromechanical model of the left atrium that combines physiological fidelity with substantially reduced computational cost. By adopting quadratic through-thickness kinematics within a fully 3D constitutive framework, the proposed approach overcomes the artificial stiffening issues commonly associated with standard low-order 3D solid discretizations in thin-walled atrial geometries.

Numerical results under both physiological conditions and atrial fibrillation demonstrate that the 3D-shell model reproduces atrial deformation and pressure-volume loops with accuracy comparable to that of multi-layer 3D tetrahedral meshes, while requiring significantly lower computational cost. In particular, the numerical comparisons revealed that a single-layer tetrahedral mesh captures only about 20% of the stroke work performed during the active pumping phase, leading to a limited atrial

response and an underestimation of ventricular filling. Moreover, the 3D-shell formulation captures these compliant atrial mechanics without resorting to through-thickness mesh refinement, which is mandatory for standard 3D formulations.

These findings highlight spatial discretization as a critical numerical choice in atrial electromechanics and support the use of shell-based formulations for efficient and mechanically consistent simulations. The proposed 3D-shell model therefore provides a solid foundation for patient-specific applications and for future extensions toward multi-chamber and fluid-structure interaction frameworks.

Declarations

Competing interests. The authors declare that they have no competing interests.

Data availability. No datasets were generated or analyzed during the current study.

Funding. This work was partially supported by Bpifrance through the MEDITWIN project sustained by France 2030 program of the French Goverment. OR was partially supported by the Vicerrectoria de Investigación, Desarrollo e Innovación (VRIDEI) of the Universidad de Santiago de Chile, and the National Agency for Research and Development (ANID) Doctorado Becas Chile/2020 - 72210101 of the Government of Chile.

Authors' contributions. Conceptualization: CB, DC, MF, MV, OR. Formal analysis and investigation: CB, DC, MF, MV, OR. Funding acquisition: MF, OR. Methodology: CB, DC, MF, MV, OR. Software: CB, MF, MV, OR. Supervision: DC, MF, MV. Writing - original draft preparation: CB, OR. Writing - review and editing: CB, DC, MF, MV, OR.

Acknowledgments. The authors wish to thank Philippe Moireau (École Polytechnique) for the valuable discussions on cardiac modeling.

A Electrophysiological model

In this work, the electrical activity of the left atrium is described using the bidomain model (see, e.g., [104, 105]). Cardiac electrophysiology is hence formulated as a coupled PDE-ODE system involving the cellular ionic dynamics, a nonlinear reaction–diffusion equation for the transmembrane potential and an elliptic equation for the extracellular potential. The electrophysiological problem of the left atrium reads: Find the transmembrane potential $V_{\mathrm{m}} : \Omega \times \mathbb{R}^+ \to \mathbb{R}$, the extracellular potential $\phi_{\mathrm{e}} : \Omega \times \mathbb{R}^+ \to \mathbb{R}$ and the ionic variable $\boldsymbol{c} : \Omega \times \mathbb{R}^+ \to \mathbb{R}^{N_{\mathrm{ion}}}$ such that

$$\begin{cases} A_{\mathrm{m}}\big(C_{\mathrm{m}}\partial_t V_{\mathrm{m}} + I_{\mathrm{ion}}\left(V_{\mathrm{m}}, \boldsymbol{c}\right)\big) - \operatorname{div}\left(\boldsymbol{\sigma}_{\mathrm{i}}\boldsymbol{\nabla} V_{\mathrm{m}}\right) - \operatorname{div}\left(\boldsymbol{\sigma}_{\mathrm{i}}\boldsymbol{\nabla}\phi_{\mathrm{e}}\right) = A_{\mathrm{m}} I_{\mathrm{app}} & \text{in} \quad \Omega, \\ \operatorname{div}\big(\left(\boldsymbol{\sigma}_{\mathrm{i}} + \boldsymbol{\sigma}_{\mathrm{e}}\right)\boldsymbol{\nabla}\phi_{\mathrm{e}}\big) + \operatorname{div}\left(\boldsymbol{\sigma}_{\mathrm{i}}\boldsymbol{\nabla} V_{\mathrm{m}}\right) = 0 & \text{in} \quad \Omega, \\ \partial_t \boldsymbol{c} + \boldsymbol{g}\left(V_{\mathrm{m}}, \boldsymbol{c}\right) = \boldsymbol{0} & \text{in} \quad \Omega, \\ \boldsymbol{\sigma}_{\mathrm{i}}\boldsymbol{\nabla} V_{\mathrm{m}} \cdot \boldsymbol{n} + \boldsymbol{\sigma}_{\mathrm{i}}\boldsymbol{\nabla}\phi_{\mathrm{e}} \cdot \boldsymbol{n} = 0 & \text{on} \quad \partial\Omega, \\ (\boldsymbol{\sigma}_{\mathrm{i}} + \boldsymbol{\sigma}_{\mathrm{e}})\boldsymbol{\nabla}\phi_{\mathrm{e}} \cdot \boldsymbol{n} + \boldsymbol{\sigma}_{\mathrm{i}}\boldsymbol{\nabla} V_{\mathrm{m}} \cdot \boldsymbol{n} = 0 & \text{on} \quad \partial\Omega. \end{cases} \tag{26}$$

Here, A_{m} denotes the membrane surface/volume ratio, C_{m} is the membrane capacitance per unit area, I_{ion} represents the nonlinear ionic current describing the exchange of ions across the cell membrane, and I_{app} denotes a prescribed external stimulus current.

The ionic current I_{ion} is modeled based on the physiological ionic model proposed in [106], a widely adopted framework for simulating atrial electrical activity (see, e.g., [40, 72, 107–109]). The symbols $\boldsymbol{\sigma}_{\mathrm{i}}$ and $\boldsymbol{\sigma}_{\mathrm{e}}$ denote the intra- and extracellular conductivity tensors, respectively. The electrical conductivity properties of cardiac tissue are inherently anisotropic, exhibiting higher values along the fiber orientation compared to the transverse plane. This anisotropic behavior is incorporated into the conductivity tensors through the following relation:

$$\boldsymbol{\sigma}_{\mathrm{i}} \stackrel{\mathrm{def}}{=} \sigma_{\mathrm{i}}^{\mathrm{t}}\mathbb{I} + \left(\sigma_{\mathrm{i}}^{\mathrm{l}} - \sigma_{\mathrm{i}}^{\mathrm{t}}\right)\boldsymbol{f}\otimes\boldsymbol{f}, \quad \boldsymbol{\sigma}_{\mathrm{e}} \stackrel{\mathrm{def}}{=} \sigma_{\mathrm{e}}^{\mathrm{t}}\mathbb{I} + \left(\sigma_{\mathrm{e}}^{\mathrm{l}} - \sigma_{\mathrm{e}}^{\mathrm{t}}\right)\boldsymbol{f}\otimes\boldsymbol{f},$$

where $\boldsymbol{f}$, as in Section 2.1, stands for the unit vector aligned with the fiber direction, $\mathbb{I}$ is the identity matrix and σ_k^{l} and σ_k^{t}, with $k \in \{\mathrm{i},\mathrm{e}\}$, are the conductivity coefficients along and transverse to the fiber, respectively. The Neumann boundary conditions

Parameter	Conductivity	Tissue	BB	FO	Unit
σ_i^t	Interior transverse direction	$2.2 \cdot 10^{-4}$	$1.045 \cdot 10^{-3}$	$2.2 \cdot 10^{-4}$	$\mathrm{S\,cm^{-1}}$
σ_i^l	Interiopr longitudinal direction	$2.2 \cdot 10^{-3}$	$1.639 \cdot 10^{-3}$	$2.2 \cdot 10^{-3}$	$\mathrm{S\,cm^{-1}}$
σ_e^t	Exterior transverse direction	$9.0 \cdot 10^{-4}$	$4.275 \cdot 10^{-3}$	$9.0 \cdot 10^{-4}$	$\mathrm{S\,cm^{-1}}$
σ_e^l	Exterior longitudinal direction	$2.2 \cdot 10^{-3}$	$1.435 \cdot 10^{-3}$	$2.07 \cdot 10^{-4}$	$\mathrm{S\,cm^{-1}}$

Table 5: Conductivity values of the electrophysiological simulations. BB: Banchmann bundle. FO: Fossa ovalis.

$(26)_{4,5}$ enforce that the left atrium is electrically isolated, that is, the intracellular and extracellular currents vanish on its boundary Ω. As the bidomain formulation (26) defines ϕ_{e} only up to an additive constant, a unique solution is obtained by imposing, for instance, the zero-mean constraint $\int_\Omega \phi_{\mathrm{e}} = 0$.

B Atrial fiber generation

The fiber architecture of the left atrium is modeled using a surface-based adaptation of the Laplace-Dirichlet Rule-Based (LDRB) framework proposed in [16]. To capture the significant transmural heterogeneity observed between the inner and outer layers [68, 110], the algorithm is applied separately to the endocardial Γ_{en} and epicardial Γ_{ep} surfaces, rather than solving for a single volumetric field.

First, each surface is partitioned into anatomically relevant boundaries, including the pulmonary vein rings, the mitral annulus, and the appendage apex. These boundaries serve as Dirichlet constraints for a set of harmonic potentials Ψ_j (where $j \in \{\mathrm{en},\mathrm{ep}\}$), governed by the surface Laplace-Beltrami operator. The gradients of

these scalar fields define the local fiber direction for specific anatomical bundles. Distinct regions, such as the circular fibers surrounding the pulmonary veins or the longitudinal structures of the septal wall, are identified through threshold-based selection rules adapted from [16]. Notably, the epicardial definition includes a specific correction for the Bachmann's Bundle to ensure fibers align parallel to the mitral valve ring, contrasting with the orientation of the underlying endocardium.

Once the fiber orientations are determined on both surfaces, the full 3D fiber architecture is constructed via transmural interpolation. Following the approach in [69], the fiber vector $\boldsymbol{f}$ at any point across the wall thickness is defined as

$$\boldsymbol{f}(\xi^1,\xi^2,\xi^3) \stackrel{\text{def}}{=} \boldsymbol{f}_0(\xi^1,\xi^2)\cos\left(\frac{2\theta(\xi^1,\xi^2)\xi^3}{\epsilon(\xi^1,\xi^2)}\right) + \boldsymbol{f}_0^{\perp}(\xi^1,\xi^2)\sin\left(\frac{2\theta(\xi^1,\xi^2)\xi^3}{\epsilon(\xi^1,\xi^2)}\right).$$

where $\boldsymbol{f}_0$ denotes the fiber orientation at the mid-surface of the left atrium, which lies in the tangential plane, and $\boldsymbol{f}_0^{\perp}$ is the fiber orthogonal to $\boldsymbol{f}_0$, also within the tangential plane. Additionally, ϵ represents the thickness of the left atrium at a given point, and θ is half the angle between the fibers in the epicardium and endocardium, as illustrated in Fig. 16. The resulting fiber distribution is illustrated in Fig. 5b.

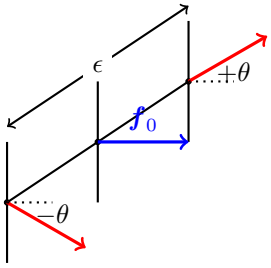

Fig. 16: Angle variation across the thickness of the left atrium.

References

[1] Trayanova, N.A., Winslow, R.: Whole-heart modeling. Circulation Research **108**(1), 113–128 (2011)

[2] Chabiniok, R., Wang, V.Y., Hadjicharalambous, M., Asner, L., Lee, J., Sermesant, M., Kuhl, E., Young, A.A., Moireau, P., Nash, M.P., Chapelle, D., Nordsletten, D.A.: Multiphysics and multiscale modelling, data–model fusion and integration of organ physiology in the clinic: ventricular cardiac mechanics. Interface Focus **6**(2), 20150083 (2016)

[3] Niederer, S.A., Lumens, J., Trayanova, N.A.: Computational models in cardiology. Nature reviews cardiology **16**(2), 100–111 (2019)

[4] Corral-Acero, J., Margara, F., Marciniak, M., Rodero, C., Loncaric, F., Feng, Y., Gilbert, A., Fernandes, J.F., Bukhari, H.A., Wajdan, A., Martinez, M.V., Santos, M.S., Shamohammdi, M., Luo, H., Westphal, P., Leeson, P., DiAchille, P., Gurev, V., Mayr, M., Geris, L., Pathmanathan, P., Morrison, T., Cornelussen, R., Prinzen, F., Delhaas, T., Doltra, A., Sitges, M., Vigmond, E.J., Zacur, E., Grau, V., Rodriguez, B., Remme, E.W., Niederer, S., Mortier, P., McLeod, K., Potse, M., Pueyo, E., Bueno-Orovio, A., Lamata, P.: The 'digital twin' to enable the vision of precision cardiology. European Heart Journal **41**(48), 4556–4564 (2020)

[5] Peirlinck, M., Costabal, F.S., Yao, J., Guccione, J., Tripathy, S., Wang, Y., Ozturk, D., Segars, P., Morrison, T., Levine, S., *et al.*: Precision medicine in human heart modeling: Perspectives, challenges, and opportunities. Biomechanics and modeling in mechanobiology **20**, 803–831 (2021)

[6] Bishop, M., Rajani, R., Plank, G., Gaddum, N., Carr-White, G., Wright, M., O'Neill, M., Niederer, S.: Three-dimensional atrial wall thickness maps to inform catheter ablation procedures for atrial fibrillation. EP Europace **18**(3), 376–383 (2015)

[7] Whitaker, J., Rajani, R., Chubb, H., Gabrawi, M., Varela, M., Wright, M., Niederer, S., O'Neill, M.D.: The role of myocardial wall thickness in atrial arrhythmogenesis. EP Europace **18**(12), 1758–1772 (2016)

[8] Hoermann, J.M., Pfaller, M.R., Avena, L., Bertoglio, C., Wall, W.A.: Automatic mapping of atrial fiber orientations for patient-specific modeling of cardiac electromechanics using image registration. International Journal for Numerical Methods in Biomedical Engineering **35**(6), 3190 (2019)

[9] Seemann, G., Höper, C., Sachse, F.B., Dössel, O., Holden, A.V., Zhang, H.: Heterogeneous three-dimensional anatomical and electrophysiological model of human atria. Philosophical Transactions of the Royal Society A: Mathematical, Physical and Engineering Sciences **364**(1843), 1465–1481 (2006)

[10] Plank, G., Prassl, A., Hofer, E., Trayanova, N.A.: Evaluating intramural virtual electrodes in the myocardial wedge preparation: Simulations of experimental conditions. Biophysical Journal **94**(5), 1904–1915 (2008)

[11] Krueger, M.W., Schmidt, V., Tobón, C., Weber, F.M., Lorenz, C., Keller, D.U.J., Barschdorf, H., Burdumy, M., Neher, P., Plank, G., Rhode, K., Seemann, G., Sanchez-Quintana, D., Saiz, J., Razavi, R., Dössel, O.: Modeling atrial fiber orientation in patient-specific geometries: A semi-automatic rule-based approach. In: Metaxas, D.N., Axel, L. (eds.) Functional Imaging and Modeling of the Heart, pp. 223–232. Springer, Berlin, Heidelberg (2011)

[12] Labarthe, S., Coudiere, Y., Henry, J., Cochet, H.: A semi-automatic method to construct atrial fibre structures: A tool for atrial simulations. In: 2012

Computing in Cardiology, pp. 881–884 (2012)

[13] Tobón, C., Ruiz-Villa, C.A., Heidenreich, E., Romero, L., Hornero, F., Saiz, J.: A three-dimensional human atrial model with fiber orientation. electrograms and arrhythmic activation patterns relationship. PLOS ONE **8**(2), 1–13 (2013)

[14] Ferrer, A., Sebastián, R., Sánchez-Quintana, D., Rodríguez, J.F., Godoy, E.J., Martínez, L., Saiz, J.: Detailed anatomical and electrophysiological models of human atria and torso for the simulation of atrial activation. PLOS ONE **10**(11), 1–29 (2015)

[15] Rocher, S., López, A., Ferrer, A., Martínez, L., Sánchez, D., Saiz, J.: A highly-detailed 3d model of the human atria. In: Lhotska, L., Sukupova, L., Lacković, I., Ibbott, G.S. (eds.) World Congress on Medical Physics and Biomedical Engineering 2018, pp. 649–653. Springer, Singapore (2019)

[16] Piersanti, R., Africa, P.C., Fedele, M., Vergara, C., Dedè, L., Corno, A.F., Quarteroni, A.: Modeling cardiac muscle fibers in ventricular and atrial electrophysiology simulations. Computer Methods in Applied Mechanics and Engineering **373**, 113468 (2021)

[17] Usyk, T.P., LeGrice, I.J., McCulloch, A.D.: Computational model of three-dimensional cardiac electromechanics. Computing and Visualization in Science **4**(4), 249–257 (2002)

[18] Smith, N.P., Nickerson, D.P., Crampin, E.J., Hunter, P.J.: Multiscale computational modelling of the heart. Acta Numerica **13**, 371–431 (2004)

[19] Crampin, E.J., Halstead, M., Hunter, P., Nielsen, P., Noble, D., Smith, N., Tawhai, M.: Computational physiology and the physiome project. Experimental Physiology **89**(1), 1–26 (2004)

[20] Chapelle, D., Fernández, M.A., Gerbeau, J.-F., Moireau, P., Sainte-Marie, J., Zemzemi, N.: Numerical simulation of the electromechanical activity of the heart. In: International Conference on Functional Imaging and Modeling of the Heart, pp. 357–365 (2009). Springer

[21] Göktepe, S., Kuhl, E.: Electromechanics of the heart: a unified approach to the strongly coupled excitation–contraction problem. Computational Mechanics **45**(2), 227–243 (2010)

[22] Nordsletten, D.A., Niederer, S.A., Nash, M.P., Hunter, P.J., Smith, N.P.: Coupling multi-physics models to cardiac mechanics. Progress in Biophysics and Molecular Biology **104**(1), 77–88 (2011)

[23] Chapelle, D., Le Tallec, P., Moireau, P., Sorine, M.: Energy-preserving muscle tissue model: formulation and compatible discretizations. International Journal

for Multiscale Computational Engineering **10**(2) (2012)

[24] Sermesant, M., Chabiniok, R., Chinchapatnam, P., Mansi, T., Billet, F., Moireau, P., Peyrat, J.M., Wong, K., Relan, J., Rhode, K., Ginks, M., Lambiase, P., Delingette, H., Sorine, M., Rinaldi, C.A., Chapelle, D., Razavi, R., Ayache, N.: Patient-specific electromechanical models of the heart for the prediction of pacing acute effects in CRT: A preliminary clinical validation. Medical Image Analysis **16**(1), 201–215 (2012)

[25] Hirschvogel, M., Bassilious, M., Jagschies, L., Wildhirt, S.M., Gee, M.W.: A monolithic 3d-0d coupled closed-loop model of the heart and the vascular system: Experiment-based parameter estimation for patient-specific cardiac mechanics. International Journal for Numerical Methods in Biomedical Engineering **33**(8), 2842 (2017)

[26] Garcia-Blanco, E., Ortigosa, R., Gil, A.J., Bonet, J.: Towards an efficient computational strategy for electro-activation in cardiac mechanics. Computer Methods in Applied Mechanics and Engineering **356**, 220–260 (2019)

[27] Augustin, C.M., Gsell, M.A.F., Karabelas, E., Willemen, E., Prinzen, F.W., Lumens, J., Vigmond, E.J., Plank, G.: A computationally efficient physiologically comprehensive 3d–0d closed-loop model of the heart and circulation. Computer Methods in Applied Mechanics and Engineering **386**, 114092 (2021)

[28] Piersanti, R., Regazzoni, R., Salvador, S., Corno, A.F., Dede', L., Vergara, C., Quarteroni, A.: 3D–0D closed-loop model for the simulation of cardiac biventricular electromechanics. Computer Methods in Applied Mechanics and Engineering **391**, 114607 (2022)

[29] Di Martino, E.S., Bellini, C., Schwartzman, D.S.: In vivo porcine left atrial wall stress: Computational model. Journal of Biomechanics **44**(15), 2589–2594 (2011)

[30] Fritz, T., Wieners, C., Seemann, G., Steen, H., Dössel, O.: Simulation of the contraction of the ventricles in a human heart model including atria and pericardium. Biomechanics and Modeling in Mechanobiology **13**(3), 627–641 (2014)

[31] Augustin, C.M., Neic, A., Liebmann, M., Prassl, A.A., Niederer, S.A., Haase, G., Plank, G.: Anatomically accurate high resolution modeling of human whole heart electromechanics: A strongly scalable algebraic multigrid solver method for nonlinear deformation. Journal of Computational Physics **305**, 622–646 (2016)

[32] Strocchi, M., Gsell, M.A.F., Augustin, C.M., Razeghi, O., Roney, C.H., Prassl, A.J., Vigmond, E.J., Behar, J.M., Gould, J.S., Rinaldi, C.A., Bishop, M.J., Plank, G., Niederer, S.A.: Simulating ventricular systolic motion in a four-chamber heart model with spatially varying robin boundary conditions to model

the effect of the pericardium. Journal of Biomechanics **101**, 109645 (2020)

[33] Satriano, A., Vigmond, E.J., Schwartzman, D.S., Di Martino, E.S.: Mechano-electric finite element model of the left atrium. Computers in Biology and Medicine **96**, 24–31 (2018)

[34] Feng, L., Gao, H., Griffith, B., Niederer, S., Luo, X.: Analysis of a coupled fluid-structure interaction model of the left atrium and mitral valve. International Journal for Numerical Methods in Biomedical Engineering **35**(11), 3254 (2019)

[35] Land, S., Niederer, S.A.: Influence of atrial contraction dynamics on cardiac function. International journal for numerical methods in biomedical engineering **34**(3), 2931 (2018)

[36] Pfaller, M.R., Hörmann, J.M., Weigl, M., Nagler, A., Chabiniok, R., Bertoglio, C., Wall, W.A.: The importance of the pericardium for cardiac biomechanics: from physiology to computational modeling. Biomechanics and modeling in mechanobiology **18**, 503–529 (2019)

[37] Augustin, C.M., Fastl, T.E., Neic, A., Bellini, C., Whitaker, J., Rajani, R., O'Neill, M.D., Bishop, M.J., Plank, G., Niederer, S.A.: The impact of wall thickness and curvature on wall stress in patient-specific electromechanical models of the left atrium. Biomechanics and modeling in mechanobiology **19**(3), 1015–1034 (2020)

[38] Baillargeon, B., Rebelo, N., Fox, D.D., Taylor, R.L., Kuhl, E.: The living heart project: A robust and integrative simulator for human heart function. European Journal of Mechanics - A/Solids **48**, 38–47 (2014). Frontiers in Finite-Deformation Electromechanics

[39] Gerach, T., Schuler, S., Fröhlich, J., Lindner, L., Kovacheva, E., Moss, R., Wülfers, E.M., Seemann, G., Wieners, C., Loewe, A.: Electro-mechanical whole-heart digital twins: a fully coupled multi-physics approach. Mathematics **9**(11), 1247 (2021)

[40] Fedele, M., Piersanti, R., Regazzoni, F., Salvador, M., Africa, P.C., Bucelli, M., Zingaro, A., Quarteroni, A., *et al.*: A comprehensive and biophysically detailed computational model of the whole human heart electromechanics. Computer Methods in Applied Mechanics and Engineering **410**, 115983 (2023)

[41] Feng, L., Gao, H., Luo, X.: Whole-heart modelling with valves in a fluid–structure interaction framework. Computer Methods in Applied Mechanics and Engineering **420**, 116724 (2024)

[42] Gonzalo, A., Augustin, C.M., Bifulco, S.F., Telle, A., Chahine, Y., Kassar, A., Guerrero-Hurtado, M., Durán, E., Martínez-Legazpi, P., Flores, O., Bermejo, J., Plank, G., Akoum, N., Boyle, P.M., Alamo, J.C.: Multiphysics simulations

reveal haemodynamic impacts of patient-derived fibrosis-related changes in left atrial tissue mechanics. The Journal of Physiology **602**(24), 6789–6812 (2024)

[43] Viola, F., Del Corso, G., Verzicco, R.: High-fidelity model of the human heart: An immersed boundary implementation. Phys. Rev. Fluids **8**, 100502 (2023)

[44] Telle, A., Kassar, A., Chamoun, N., Haykal, R., Gonzalo, A., Hensley, T., Chahine, Y., Flores, O., Alamo, J.C., Akoum, N., Augustin, C.M., Boyle, P.M.: Systematic computational assessment of atrial function impairment due to fibrotic remodeling in electromechanical properties. PLOS Computational Biology **21**(12), 1–33 (2025)

[45] Arjoune, T., Bilas, C., Meierhofer, C., Stern, H., Ewert, P., Gee, M.W.: Inverse analysis of patient-specific parameters of a 3d–0d closed-loop cardiovascular model with an exemplary application to an adult tetralogy of fallot case. Biomechanics and Modeling in Mechanobiology **24**(6), 2039–2068 (2025)

[46] Shi, L., Gan, B., Chen, I.Y., Vedula, V.: Personalized multiscale modeling of left atrial mechanics and blood flow. Computer Methods in Applied Mechanics and Engineering **448**, 118412 (2026)

[47] Chapelle, D., Bathe, K.-J.: The Finite Element Analysis of Shells - Fundamentals, 2nd edn. Computational Fluid and Solid Mechanics, p. 410. Springer, Berlin, Heidelberg (2011). https://doi.org/10.1007/978-3-642-16408-8

[48] Chapelle, D., Ferent, A., Bathe, K.J.: 3D-shell elements and their underlying mathematical model. Mathematical Models and Methods in Applied Sciences **14**(01), 105–142 (2004)

[49] Bathe, K.-J., Iosilevich, A., Chapelle, D.: An evaluation of the MITC shell elements. Computers & Structures **75**(1), 1–30 (2000)

[50] Caruel, M., Chabiniok, R., Moireau, P., Lecarpentier, Y., Chapelle, D.: Dimensional reductions of a cardiac model for effective validation and calibration. Biomechanics and modeling in mechanobiology **13**(4), 897–914 (2014)

[51] Ruz, O., Vidrascu, M., Chapelle, D., Fernández, M.A.: 3d-shell electromechanical modeling of the left atrium. In: International Conference on Functional Imaging and Modeling of the Heart, pp. 48–59 (2025). Springer

[52] Feng, L., Gao, H., Qi, N., Danton, M., Hill, N.A., Luo, X.: Fluid–structure interaction in a fully coupled three-dimensional mitral–atrium–pulmonary model. Biomechanics and modeling in mechanobiology **20**(4), 1267–1295 (2021)

[53] Demiray, H.: A note on the elasticity of soft biological tissues. Journal of biomechanics **5**(3), 309–311 (1972)

[54] Gasser, T.C., Ogden, R.W., Holzapfel, G.A.: Hyperelastic modelling of arterial layers with distributed collagen fibre orientations. Journal of the royal society interface **3**(6), 15–35 (2006)

[55] Kimmig, F., Chapelle, D., Moireau, P.: Thermodynamic properties of muscle contraction models and associated discrete-time principles. Advanced Modeling and Simulation in Engineering Sciences **6**(1), 1–36 (2019)

[56] Bestel, J., Clément, F., Sorine, M.: A biomechanical model of muscle contraction. In: International Conference on Medical Image Computing and Computer-Assisted Intervention, pp. 1159–1161 (2001). Springer

[57] Holzapfel, G.A., Ogden, R.W.: Constitutive modelling of passive myocardium: a structurally based framework for material characterization. Philosophical Transactions of the Royal Society A: Mathematical, Physical and Engineering Sciences **367**(1902), 3445–3475 (2009)

[58] Hart, J.: Normal resting pulse rate ranges. Journal of Nursing Education and Practice **5**(8), 95–98 (2015)

[59] Sussman, T., Bathe, K.-J.: 3d-shell elements for structures in large strains. Computers & structures **122**, 2–12 (2013)

[60] Chapelle, D., Paris, I.: Detailed reliability assessment of triangular MITC elements for thin shells. Computers & Structures **86**(23), 2192–2202 (2008)

[61] Jeon, H.-M., Lee, P.-S., Bathe, K.-J.: The mitc3 shell finite element enriched by interpolation covers. Computers & Structures **134**, 128–142 (2014)

[62] Jeon, H.-M., Lee, Y., Lee, P.-S., Bathe, K.-J.: The mitc3+ shell element in geometric nonlinear analysis. Computers & Structures **146**, 91–104 (2015)

[63] Sainte-Marie, J., Chapelle, D., Cimrman, R., Sorine, M.: Modeling and estimation of the cardiac electromechanical activity. Computers & Structures **84**(28), 1743–1759 (2006)

[64] Besl, P.J., McKay, N.D.: Method for registration of 3-d shapes. In: Sensor Fusion IV: Control Paradigms and Data Structures, vol. 1611, pp. 586–606 (1992). Spie

[65] Gee, M.W., Förster, C., Wall, W.: A computational strategy for prestressing patient-specific biomechanical problems under finite deformation. International Journal for Numerical Methods in Biomedical Engineering **26**(1), 52–72 (2010)

[66] Moireau, P., Xiao, N., Astorino, M., Figueroa, C.A., Chapelle, D., Taylor, C.A., Gerbeau, J.-F.: External tissue support and fluid–structure simulation in blood flows. Biomechanics and modeling in mechanobiology **11**, 1–18 (2012)

[67] Ho, S.Y., Cabrera, J.A., Sanchez-Quintana, D.: Left atrial anatomy revisited.

Circulation: Arrhythmia and Electrophysiology **5**(1), 220–228 (2012)

[68] Pashakhanloo, F., Herzka, D.A., Ashikaga, H., Mori, S., Gai, N., Bluemke, D.A., Trayanova, N.A., McVeigh, E.R.: Myofiber architecture of the human atria as revealed by submillimeter diffusion tensor imaging. Circulation: arrhythmia and electrophysiology **9**(4), 004133 (2016)

[69] Chapelle, D., Collin, A., Gerbeau, J.-F.: A surface-based electrophysiology model relying on asymptotic analysis and motivated by cardiac atria modeling. Math. Models Methods Appl. Sci. **23**(14), 2749–2776 (2013)

[70] Porumbescu, S.D., Budge, B., Feng, L., Joy, K.I.: Shell maps. ACM Transactions on Graphics (TOG) **24**(3), 626–633 (2005)

[71] Zhao, J., Stephenson, R.S., Sands, G.B., LeGrice, I.J., Zhang, H., Jarvis, J.C., Smaill, B.H.: Atrial fibrosis and atrial fibrillation: a computer simulation in the posterior left atrium. In: Functional Imaging and Modeling of the Heart: 7th International Conference, FIMH 2013, London, UK, June 20-22, 2013. Proceedings 7, pp. 400–408 (2013). Springer

[72] Schenone, E., Collin, A., Gerbeau, J.-F.: Numerical simulation of electrocardiograms for full cardiac cycles in healthy and pathological conditions. International journal for numerical methods in biomedical engineering **32**(5), 02744 (2016)

[73] Pagel, P.S., Kehl, F., Gare, M., Hettrick, D.A., Kersten, J.R., Warltier, D.C.: Mechanical function of the left atrium: new insights based on analysis of pressure-volume relations and doppler echocardiography. Anesthesiology **98**(4), 975–994 (2003)

[74] Stöcker, Y., Guerrero-Hurtado, M., Durán, E., Gonzalo, A., Ristić, Z., Telle, Å., Kassar, A., Haykal, R., Akoum, N., Boyle, P.M., et al.: Effect of wall motion sampling on cfd-derived left atrial flow metrics. bioRxiv, 2025–10 (2025)

[75] Kistler, P.M., Sanders, P., Fynn, S.P., Stevenson, I.H., Spence, S.J., Vohra, J.K., Sparks, P.B., Kalman, J.M.: Electrophysiologic and electroanatomic changes in the human atrium associated with age. Journal of the American College of Cardiology **44**(1), 109–116 (2004)

[76] Roşca, M., Lancellotti, P., Popescu, B.A., Piérard, L.A.: Left atrial function: pathophysiology, echocardiographic assessment, and clinical applications. Heart **97**(23), 1982–1989 (2011)

[77] Abhayaratna, W.P., Seward, J.B., Appleton, C.P., Douglas, P.S., Oh, J.K., Tajik, A.J., Tsang, T.S.: Left atrial size: physiologic determinants and clinical applications. Journal of the American College of Cardiology **47**(12), 2357–2363 (2006)

[78] Iaizzo, P.A. (ed.): Handbook of Cardiac Anatomy, Physiology, and Devices, 4th edn., p. 1009. Springer, Cham, Switzerland (2024). https://doi.org/10.1007/978-3-031-72581-4

[79] Sánchez-Quintana, D., Doblado-Calatrava, M., Cabrera, J.A., Macías, Y., Saremi, F.: Anatomical basis for the cardiac interventional electrophysiologist. BioMed Research International **2015**(1), 547364 (2015)

[80] Sugimoto, T., Robinet, S., Dulgheru, R., Bernard, A., Ilardi, F., Contu, L., Addetia, K., Caballero, L., Kacharava, G., Athanassopoulos, G.D., *et al.*: Echocardiographic reference ranges for normal left atrial function parameters: results from the eacvi norre study. European Heart Journal-Cardiovascular Imaging **19**(6), 630–638 (2018)

[81] Jalife, J.: Rotors and spiral waves in atrial fibrillation. Journal of cardiovascular electrophysiology **14**(7), 776–780 (2003)

[82] Adeniran, I., MacIver, D.H., Garratt, C.J., Ye, J., Hancox, J.C., Zhang, H.: Effects of persistent atrial fibrillation-induced electrical remodeling on atrial electro-mechanics–insights from a 3d model of the human atria. PloS one **10**(11), 0142397 (2015)

[83] Alonso, S., Bär, M., Echebarria, B.: Nonlinear physics of electrical wave propagation in the heart: a review. Reports on Progress in Physics **79**(9), 096601 (2016)

[84] Pagani, S., Dede', L., Frontera, A., Salvador, M., Limite, L., Manzoni, A., Lipartiti, F., Tsitsinakis, G., Hadjis, A., Della Bella, P., *et al.*: A computational study of the electrophysiological substrate in patients suffering from atrial fibrillation. Frontiers in Physiology **12**, 673612 (2021)

[85] Corti, M., Zingaro, A., Quarteroni, A.M., *et al.*: Impact of atrial fibrillation on left atrium haemodynamics: A computational fluid dynamics study. Computers in Biology and Medicine **150**, 106143 (2022)

[86] Suga, H.: Importance of atrial compliance in cardiac performance. Circulation research **35**(1), 39–43 (1974)

[87] Hoit, B.D., Shao, Y., Tsai, L.-M., Patel, R., Gabel, M., Walsh, R.A.: Altered left atrial compliance after atrial appendectomy. influence on left atrial and ventricular filling. Circulation research **72**(1), 167–175 (1993)

[88] Nagano, T., Arakawa, M., Tanaka, T., Yamaguchi, M., Takaya, T., Noda, T., Miwa, H., Kagawa, K., Hirakawa, S.: Diastolic compliance of the left atrium in man: a determinant of preload of the left ventricle. Heart and vessels **5**(1), 25–32 (1989)

[89] Inciardi, R.M., Rossi, A.: Left atrium: a forgotten biomarker and a potential target in cardiovascular medicine. Journal of Cardiovascular Medicine **20**(12), 797–808 (2019)

[90] Aguirre, A., Codina, R., Baiges, J., Castañar, I.: Stress–displacement stabilized finite element analysis of thin structures using solid-shell elements, part ii: Finite strain hyperelasticity. Finite Elements in Analysis and Design **236**, 104179 (2024)

[91] Trayanova, N.A., Prakosa, A.: Up digital and personal: How heart digital twins can transform heart patient care. Heart Rhythm **21**(1), 89–99 (2024)

[92] Karakasis, P., Antoniadis, A.P., Theofilis, P., Vlachakis, P.K., Milaras, N., Patoulias, D., Karamitsos, T., Fragakis, N.: Digital twin models in atrial fibrillation: Charting the future of precision therapy? Journal of Personalized Medicine **15**(6), 256 (2025)

[93] Saiz-Vivó, M., Mill, J., Iriart, X., Cochet, H., Piella, G., Sermesant, M., Camara, O.: Digital twin integrating clinical, morphological and hemodynamic data to identify stroke risk factors. npj Digital Medicine **8**(1), 369 (2025)

[94] Hoit, B.D.: Left atrial size and function: role in prognosis. Journal of the American College of Cardiology **63**(6), 493–505 (2014)

[95] Sel, K., Osman, D., Zare, F., Masoumi Shahrbabak, S., Brattain, L., Hahn, J.-O., Inan, O.T., Mukkamala, R., Palmer, J., Paydarfar, D., *et al.*: Building digital twins for cardiovascular health: From principles to clinical impact. Journal of the American Heart Association **13**(19), 031981 (2024)

[96] Nishimura, R.: Constrictive pericarditis in the modern era: a diagnostic dilemma. Heart **86**(6), 619–623 (2001)

[97] Vedula, V., George, R., Younes, L., Mittal, R.: Hemodynamics in the left atrium and its effect on ventricular flow patterns. Journal of biomechanical engineering **137**(11), 111003 (2015)

[98] Koizumi, R., Funamoto, K., Hayase, T., Kanke, Y., Shibata, M., Shiraishi, Y., Yambe, T.: Numerical analysis of hemodynamic changes in the left atrium due to atrial fibrillation. Journal of biomechanics **48**(3), 472–478 (2015)

[99] Masci, A., Barone, L., Dedè, L., Fedele, M., Tomasi, C., Quarteroni, A., Corsi, C.: The impact of left atrium appendage morphology on stroke risk assessment in atrial fibrillation: a computational fluid dynamics study. Frontiers in physiology **9**, 1938 (2019)

[100] Feng, L., Gao, H., Griffith, B., Niederer, S., Luo, X.: Analysis of a coupled fluid-structure interaction model of the left atrium and mitral valve. International

journal for numerical methods in biomedical engineering **35**(11), 3254 (2019)

[101] Bucelli, M., Zingaro, A., Africa, P.C., Fumagalli, I., Dede', L., Quarteroni, A.: A mathematical model that integrates cardiac electrophysiology, mechanics, and fluid dynamics: Application to the human left heart. International journal for numerical methods in biomedical engineering **39**(3), 3678 (2023)

[102] Bucelli, M., Dede, L.: Coupling models of resistive valves to muscle mechanics in cardiac fluid–structure interaction simulations. International Journal for Numerical Methods in Biomedical Engineering **41**(12), 70119 (2025)

[103] Ruz Núñez, O.: Mathematical modeling and numerical simulation of left heart hemodynamics with fluid-structure interaction. PhD thesis, Sorbonne Université (2025). https://theses.hal.science/tel-04973025

[104] Sundnes, J., Lines, G.T., Cai, X., Nielsen, B.F., Mardal, K.-A., Tveito, A.: Computing the Electrical Activity in the Heart. Monographs in Computational Science and Engineering, vol. 1. Springer, Berlin, Heidelberg (2006)

[105] Neu, J.C., Krassowska, W.: Homogenization of syncytial tissues. Critical reviews in biomedical engineering **21**(2), 137–199 (1993)

[106] Courtemanche, M., Ramirez, R.J., Nattel, S.: Ionic mechanisms underlying human atrial action potential properties: insights from a mathematical model. American Journal of Physiology-Heart and Circulatory Physiology **275**(1), 301–321 (1998)

[107] Dössel, O., Krueger, M.W., Weber, F.M., Wilhelms, M., Seemann, G.: Computational modeling of the human atrial anatomy and electrophysiology. Medical & biological engineering & computing **50**, 773–799 (2012)

[108] Collin, A., Gerbeau, J.-F., Hocini, M., Haïssaguerre, M., Chapelle, D.: Surface-based electrophysiology modeling and assessment of physiological simulations in atria. In: Functional Imaging and Modeling of the Heart: 7th International Conference, FIMH 2013, London, UK, June 20-22, 2013. Proceedings 7, pp. 352–359 (2013). Springer

[109] Trayanova, N.A., Lyon, A., Shade, J., Heijman, J.: Computational modeling of cardiac electrophysiology and arrhythmogenesis: toward clinical translation. Physiological Reviews **104**(3), 1265–1333 (2024)

[110] Ho, S., Sánchez-Quintana, D.: The importance of atrial structure and fibers. Clinical Anatomy: The Official Journal of the American Association of Clinical Anatomists and the British Association of Clinical Anatomists **22**(1), 52–63 (2009)